A&A 413, 843–859 (2004)
DOI: 10.1051/0004-6361:20031532

Astronomy & Astrophysics

ISO deep far-infrared survey in the "Lockman Hole"⋆

III. Catalogs and source counts at 90 & 170 μm

K. Kawara[1], H. Matsuhara[2], H. Okuda[2,3], Y. Taniguchi[4], Y. Sato[1], Y. Sofue[1], K. Wakamatsu[5], S. Oyabu[1], D. B. Sanders[6], and L. L. Cowie[6]

[1] Institute of Astronomy, The University of Tokyo, 2-21-1 Osawa, Mitaka, Tokyo, 181-0015, Japan
[2] Institute of Space and Astronautical Science (ISAS), 3-1-1 Yoshinodai, Sagamihara, Kanagawa, 229-8510, Japan
[3] Gunma Astronomical Observatory, Gunma 377-0702, Japan
[4] Astronomical Institute, Tohoku University, Aoba, Sendai 980-77, Japan
[5] Department of Physics, Gifu University, Gifu 501-11, Japan
[6] Institute for Astronomy, University of Hawaii, 2680 Woodlawn Drive, Honolulu, HI 96822, USA

Received 28 May 2003 / Accepted 25 September 2003

Abstract. We present the catalogs and source counts for the C_90 (reference wavelength of 90 μm) and C_160 (170 μm) bands, which were extracted from our analysis of an ISO deep far-infrared survey conducted as part of the Japan/UH ISO cosmology project. The total survey area is ∼0.9 deg^2 in two fields within the Lockman Hole. The analysis consists of source extraction using the IRAF DAOPHOT package and simulations carried out by adding artificial sources to the maps to estimate the detection rate, the flux bias, the positional accuracy, and the noise. The flux calibration was performed using the Sb galaxy UGC 06009 – the photometric error was estimated to be ∼50% at C_90 and ∼65% at C_160. The total noise estimated from the simulation is dominated by the confusion noise due to the high source density. The confusion noise is ∼20 mJy at C_90 and ∼35 mJy at C_160, which is much larger than the instrumental noise which is at the level of a few mJy or less. The catalogs were constructed by selecting 223 C_90 sources and 72 C_160 sources with a Signal to Noise Ratio (SNR) of three or greater. The distribution of the observed associations between C_90 and C_160 sources indicates that the 1σ positional errors are ∼20″ and ∼35″ at C_90 and C_160, respectively. The corrections for the detection rate and the flux bias are significant for sources fainter than 200 mJy at C_90 and 250 mJy at C_160. Most of the sources detected both at C_90 and C_160 have a F(C_160)/F(C_90) color redder than the Sb galaxy UGC 06009. Such a red color could result from reddening due to the flux bias or a K-correction brightening due to the effect of redshift. Red sources brighter than 200 mJy at C_160 may be very luminous galaxies like Arp 220 at moderate redshift. The source counts are derived by applying the corrections for the detection rate and flux bias. The resultant counts are quite consistent with the constraints derived from the fluctuation analysis performed in Paper II. The C_160 counts are also consistent with the results from the FIRBACK project. Our C_90 survey, which is 2–3 times deeper than those previously published, reveals an upturn in the count slope at around 200 mJy. While recent models give a reasonable fit to the C_160 counts, none of them are successful in accounting for the upturn in the C_90 counts. If the upturn is caused by ultraluminous IR galaxies, their redshifts would need to be at $z \sim 0.5$, implying a major event in galaxy evolution at moderate redshift.

Key words. galaxies: evolution – galaxies: starburst – cosmology: observations – infrared: galaxies

1. Introduction

The IRAS all-sky survey opened up a new window on galaxy evolution, and showed that a significant fraction of the bolometric luminosity of all galaxies is emitted at far-infrared wavelengths through reprocessing by dust of UV/optical light from both stars and active galactic nuclei (AGN). The far-infrared spectra of galaxies peak in the wavelength range 25–200 μm. Cirrus-dominated normal galaxies have an emission peak at 100–200 μm, while infrared-luminous starburst galaxies peak near 60 μm, and Seyfert galaxies often show a peak near 25 μm (Sanders & Mirabel 1996 and references therein). The infrared luminosity as observed by IRAS is ∼30% of the total energy output of galaxies in the local Universe (Soifer & Neugebauer 1991). The detection of the CIB (Cosmic Infrared Background) with the COBE satellite at far-infrared and submillimeter wavelengths (e.g. Puget et al. 1996) indicates that the integrated luminosity from thermal

Send offprint requests to: K. Kawara,
e-mail: kkawara@ioa.s.u-tokyo.ac.jp

⋆ Based on observations with ISO, an ESA project with instruments funded by ESA member states (especially the PI countries: France, Germany, The Netherlands, and the UK) and with the participation of ISAS and NASA.

dust emission is comparable to or greater than that of the integrated UV/optical light of galaxies in the Hubble Deep Field (HDF) (Guiderdoni et al. 1997), implying a potentially larger contribution from dust-enshrouded star formation than that inferred from the rest-frame optical/UV at high redshift. As discussed by Steidel et al. (1999 and references therein), at high redshift where optical observations are sampling the rest-frame optical/UV, the SFR density derived from optical observations (e.g. Madau et al. 1996) may be substantially underestimated as a result of absorption by dust.

The next step is to resolve the CIB into individual sources. The sub-millimeter common-user bolometer array (SCUBA) on the 15 m James Clerk Maxwell Telescope (JCMT) is now able to resolve a substantial fraction of the CIB at 0.85 mm into luminous IR galaxies most of which appear to lie at high redshift, $z > 1$ (Smail et al. 1997; Hughes et al. 1998; Barger et al. 1998; Scott et al. 2002; Sato et al. 2002). In the mid- and far-infrared, various surveys have been conducted with the European Space Agency (ESA) Infrared Space Telescope (ISO: Kessler 1996), which was in operation between 1995 and 1998. Most of the deep ISO mid-infrared surveys were performed in the 6.7 μm (LW2) and/or 15 μm (LW3) bands. 6.7 μm surveys are useful for looking at stellar systems at high redshift (Serjeant et al. 1997; Taniguchi et al. 1997; Flores et al. 1999a; Altieri et al. 1999; Sato et al. 2003; Oliver et al. 2002). The cross-identification of 6.7 μm sources with SCUBA sources suggests that star formation with a SFR of $10^3\ M_\odot\ \mathrm{yr}^{-1}$ can build up massive stellar systems of $5 \times 10^{11}\ M_\odot$ by redshift $z = 1$–2 (Sato et al. 2002). 15 μm surveys carried out by different groups to different depths, probed emission both from warm dust and the unidentified infrared bands at 6–13 μm in star forming galaxies (Serjeant et al. 1997; Flores et al. 1999b; Aussel et al. 1999; Altieri et al. 1999; Elbaz et al. 1999; Oliver et al. 2002). The 15 μm counts show an excess at 400 μJy by a factor of ∼10 (Elbaz et al. 1999), requiring strong cosmic evolution of the mid-infrared emission of galaxies. The excess could be largely attributable to bright and massive galaxies at $z < 1.5$ (Elbaz et al. 1999).

The CIB has a major peak at wavelengths 100–200 μm that is presumably due primarily to emission from cool dust (e.g., Hauser & Dwek 2001). If the rest-frame SEDs of starburst galaxies peaking at 60–100 μm are responsible, this might imply a high SFR at $z \sim 0.5$–1, corresponding to a major event in galactic evolution.

The far-infrared imaging instrument ISOPHOT (Lemke et al. 1996) onboard ISO was used to carry out deep far-infrared surveys in a ∼0.9 deg^2 area in the LH using the 90 μm and 170 μm bands (Kawara et al. 1998; Matsuhara et al. 2000), in 4 deg^2 in the Marano fields and northern ELAIS fields using the 170 μm band as part of the FIRBACK project (Puget et al. 1999; Dole et al. 2001), in 12 deg^2 of the ELIAS fields using the 90 μm band (Oliver et al. 2000; Efstathiou et al. 2000), in 0.4 deg^2 in the SA57 field using the 60 μm and 90 μm bands (Linden-Vørnle et al. 2000), and in 1.6 deg^2 in eight fields at wavelengths between 90 μm and 180 μm (Juvela et al. 2000). The far-infrared source counts derived by the various groups are in agreement with strongly evolving models of the starburst galaxy population. While the resolved sources brighter than 180 mJy at 170 μm account for less than 10% of the CIB (Dole et al. 2001), the constraints from the fluctuation analysis by Matsuhara et al. (2000) indicate that sources brighter than 35 mJy at 90 μm and 60 mJy at 170 mJy contribute 5–40% of the CIB.

This is our third paper reporting results from our ISO deep far-infrared survey that was conducted at 90 μm and 170 μm in the LH. The survey was made as part of the Japan/UH ISO cosmology program using ISAS guaranteed time. Paper I (Kawara et al. 1998), reported that the source counts at 90 μm and 170 μm are much greater than expected from a no-evolution model. The high counts at 170 μm have been confirmed by Puget et al. (1999). Paper II (Matsuhara et al. 2000), used fluctuation analysis to place constraints on the source counts down to a level of 35 mJy at 90 μm and 60 mJy at 170 μm. These constraints suggest a steep slope in the source counts versus flux, implying strong galaxy evolution, most likely at moderate redshift (e.g., Takeuchi et al. 2001). In the current paper, we describe our source extraction method, perform simulations to estimate the reliability and completeness of our survey, construct the catalogs of far-infrared sources, derive the source counts at 90 μm and 170 μm, and discuss the implications of our results.

2. Observations and Image processing

We have carried out a far-infrared survey in the LH using ISOPHOT, which was an imaging photopolarimeter onboard ISO. The LH is a region of the sky with the smallest HI column density (Lockman et al. 1986), and thus the far-infrared confusion noise caused by infrared cirrus is expected to be a minimum in this region (Gautier et al. 1992).

The survey was performed in two fields, LHEX and LHNW, between revolutions 194 and 215 (May 28 and June 19, 1996). Each field extends approximately 44′ × 44′. The center of the LHEX field is at $\alpha = 10^{\mathrm{h}}52^{\mathrm{m}}00^{\mathrm{s}}$ $\delta = +57°21'30''$ (J2000), and LHNW is at $\alpha = 10^{\mathrm{h}}33^{\mathrm{m}}55^{\mathrm{s}}$ $\delta = +57°46'20''$ (J2000). LHEX contains the field in which the ROSAT Deep Survey was carried out (Hasinger et al. 1998). Our ISOPHOT observations were made using the PHT22 raster mapping mode in the C_90 band (reference wavelength 90 μm) and the C_160 band (reference wavelength 170 μm) (see *ISO Handbook Volume V*).

Each 44′ × 44′ field consists of four rasters. The area covered by each raster is approximately 22′ × 22′. Four rasters making one field were executed and completed in a single revolution, except for LHNW at C_160, so that the position angles of all of the rasters are almost the same on the sky. For C_90, each raster has 18 × 18 raster points with raster steps of 69″ corresponding to a 1.5 pixel overlap in both directions in the spacecraft (Y, Z) coordinate system. The integration time per raster point was 16 s. Within the maximum redundancy region, each part of sky was thus observed by four different pixels resulting in a total integration time per sky position of 64 s (4 × 16 s). For C_160, each raster has 27 × 14 raster points with raster steps of 46″ corresponding to a 1.5 pixel overlap in the Y axis and raster steps of 92″ corresponding to a one pixel overlap in the Z axis. The integration time per raster

point was 20 s. Within the maximum redundancy region, each part of the sky was observed eight times by four different pixels and thus the total integration time per sky position was 160 s (8×20 s).

Our image processing consists of two stages. At the first stage, the PHT Interactive Analysis (PIA) version 7.3[1] (Gabriel et al. 1997) was used, starting with the edited raw data (ERD) created via the off-line processing version 7.0. The AOT/Batch processing mode of PIA was employed using the defaultparameters to reduce the ERD to the Astronomical Analysis Processing (AAP) level. This standard reduction includes discarding some of the readouts at the beginning of the integration ramps, linearization and deglitching of the ramps on the ERD level, signal deglitching and drift recognition at the Signal-per-Ramp Data (SRD) level, reset interval normalization, signal deglitching, dark current subtraction, and vignetting correction on the Signal-per-Chopper Plateau (SCP) data level. At the end of this stage, maps were produced at the Astronomical Analysis Processing (AAP) level in mapping mode using median brightness values. These are called AAP maps in this paper. Each AAP map corresponds to the respective $22' \times 22'$ raster.

The AAP maps, in particular for the C_90 band, are greatly affected by a slow drift in the responsivity. No sources can be recognized because of the overwhelming lattice pattern. At the second stage, we have developed the so-called median filtering technique[2] to remove the slow responsivity drift. As shown in Figs. 1 and 2 in Paper I, median filtering dramatically reduces the responsivity drift and many sources become recognizable in the map. It should be noted that the AAP C_160 map is almost identical to that from the median filtered signal map, implying that the detectors used for the C_160 band were stable and suffered little from responsivity drift.

Figure 1 shows the mosaiced maps of LHEX and LHNW, which are made from the median filtered signal. The resultant maps of the four sub-fields are first rebinned onto a 2.3″/pixel grid for C_90 and a 4.6″/pixel grid for C_160, and then combined into the $44' \times 44'$ maps. Finally, the IRAF gauss routine was applied with $\sigma = 6$ for smoothing the maps.

3. Source extraction and photometry

3.1. Source extraction

The IRAF[3] DAOPHOT package (Davis 1994) was used to extract sources from the maps for the following reasons; (1) as shown in Fig. 1, the maps are very crowded, often blending the light of two or more sources, and (2) FWHM measurements of brightness profiles of bright sources indicate that all of their FWHMs are not extended more than two detector pixels and thus they should be detected as point sources. DAOPHOT has indeed been developed to perform stellar photometry in crowded fields (Stetson 1987) such as in the cores of globular clusters. In DAOPHOT, the positions and relative magnitudes of point sources are determined by using a numerical fitting technique to match the given Point Spread Function (PSF) to the observed light distribution. Where the light of two or more sources is blended, it fits a model in which two or more of the expected PSFs are superimposed by shifting each model PSF in position and scaling in intensity until a satisfactory fit of the overall model to the image data is achieved. IRAS F10507+5723, the brightest source in our survey, was used to define the PSFs because the light distribution for IRAS F10507+5723 is typical of what is expected when a point source is observed in our survey.

The following sequence from (1) to (6) was performed for extracting sources: (1) DAOFIND was used to find sources on the original map and produce a list of x and y positions of the sources; (2) PHOT was used on the original map to obtain aperture photometry and sky values for the sources in the list; (3) ALLSTAR was used to do simultaneous PSF-fitting for all the sources found on the original map, reject poorly fitted sources, and produce a list of sources and a subtracted map from which the listed sources are subtracted; (4) DAOFIND, PHOT, and ALLSTAR were used on the subtracted maps to identify sources that had been previously hidden by brighter sources, with the procedure repeated until all the significant sources were extracted from the subtracted maps; (5) PFMERGE was used to merge the original and all the other lists obtained from the subtracted maps and produce the new merged list; (6) ALLSTAR was used on the original image to do simultaneous PSF-fitting for all the sources in the merged list and produce the final list of sources.

DAOPHOT fits the PSF to the data within the specified fitradius of 62″ for C_90 and 124″ for C_160, and computes the fitted flux and flux error. The flux error is derived from a combination of the residuals from the fitting and the uncertainty of the local sky values. The SNR for source detection is a division of the flux by the flux error, both of which DAOPHOT returns. However, such SNRs should not be regarded as true, because the flux error is calculated by using values in sub-pixels which are not themselves independent. We thus scaled the flux error in such a way that the average of the flux errors given by DAOPHOT agrees with that of the differences between the given and measured fluxes of artificial objects in simulations that will be discussed later. Figure 1 plots sources extracted by DAOPHOT on (top) the LHEX C_90 and C_160 maps and (bottom) the LHNW C_90 and C_160 maps. The detected sources have $SNR \geq 3$, which is our detection threshold in this paper.

3.2. Flux calibration

Flux scaling is done by using the same standard source as described in Paper I. This standard source is IRAS F10507+5723, which has ISO band fluxes, F(C_90) = 1218 mJy and F(C_160) = 1133 mJy. IRAS F10507+5723 is the only cataloged IRAS source in our survey fields, and it is the brightest source in our survey fields[4]. It is identified

[1] PIA is a joint development by the ESA Astrophysics Division and the ISOPHOT consortium.

[2] This routine is available in PIA at the AAP level.

[3] IRAF is distributed by NOAO, which is operated by AURA, Inc., under contract to the NSF.

[4] According to our naming convention, IRAS F10507+5723 has a C_90 name of 1EX023 and a C_160 name of 2EX021.

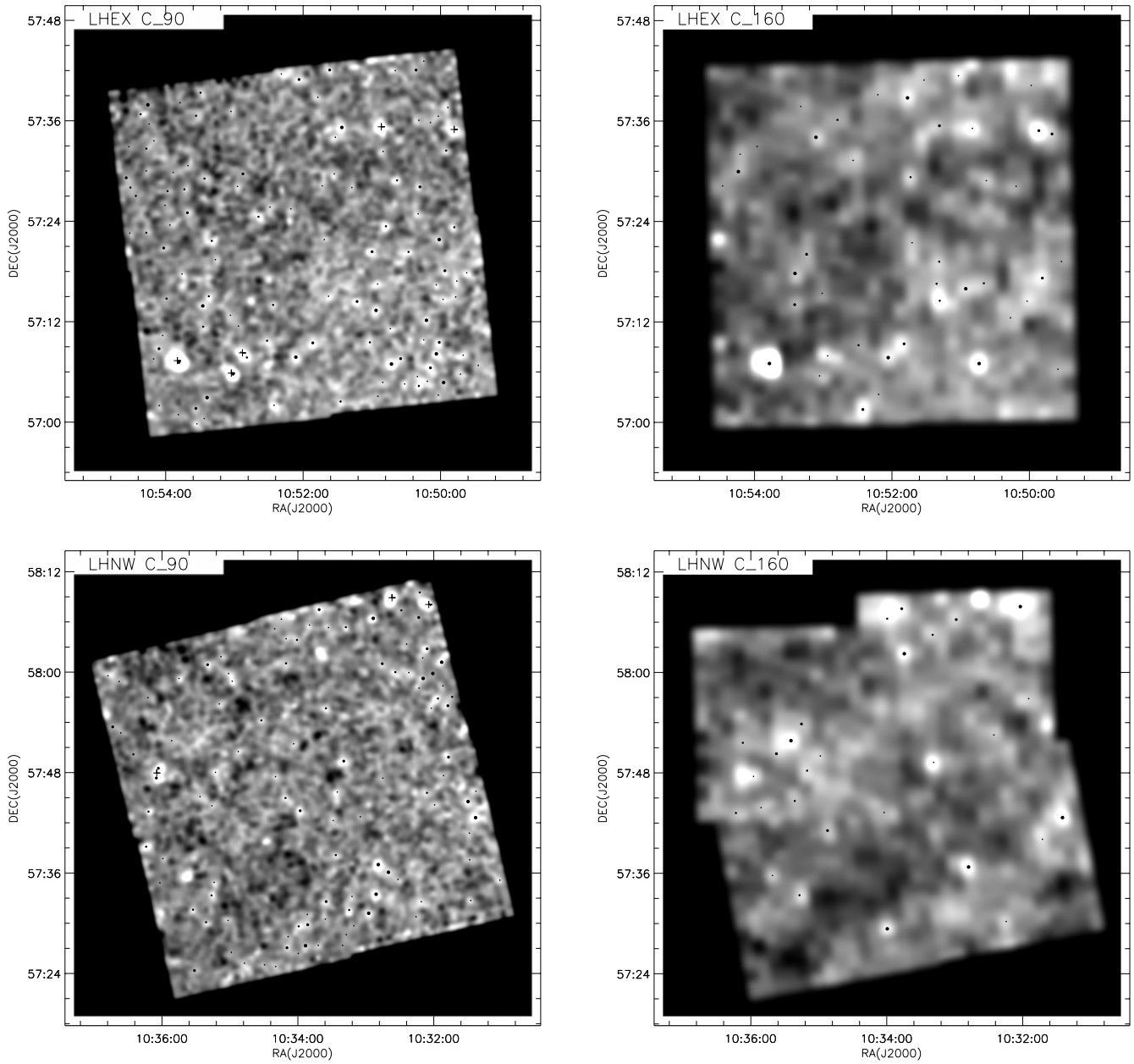

Fig. 1. The left column shows C_90 (90 μm) and C_160 (170 μm) maps of the 44′ × 44′ LHEX field, while the right column shows the same for LHNW. Each field is made up of four 22′ × 22′ sub-fields (see text). The median filtered maps have been rebinned onto a 2.3″/pixel grid for C_90 and a 4.6″/pixel grid for C_160. The IRAF GAUSS routine is then applied with σ = 6 for smoothing the images. Sources with $SNR \geq 3$ are plotted on the C_90 and C_160 maps. The SNRs are coded by the filled circles; the largest circles represent sources with $SNR > 6$, the second with SNR = 6–5, the third with SNR = 5–4, and the smallest with SNR = 4–3. Flux calibration was performed using UGC 06009(IRAS F10507+5723) which is the only cataloged IRAS source in our survey fields. It is noted that all “sources” detected within 46″ at C_90 (1/3 of the detector array) and 92″ at C_160 (1/2 of the array) from the outer bounds of the survey fields are not plotted because the sensitivity in these outer boundary regions is significantly poorer than the inner regions due to fewer redundant observations. The “+” (plus) symbols represent the sources detected by Linden-Vørnle et al. (2000).

with a Sb galaxy UGC 06009 (Thuan & Sauvage 1992). The IRAS fluxes are $F(60\ \mu\text{m})$ = 533 ± 59 mJy and $F(100\ \mu\text{m})$ = 1218 ± 292 mJy (IRAS FSC 1990). Its flux ratio, $F(100\ \mu\text{m})/F(60\ \mu\text{m})$ = 2.29, can be fit with a combination of IR cirrus and starburst spectra (Pearson & Rowan-Robinson 1996), if 76% of the 100 μm flux comes from the cirrus component. This predicts $F(\text{C\_160})/F(100\ \mu\text{m})$ = 0.93, which implies $F(\text{C\_160})$ = 1133 mJy. $F(\text{C\_90})$ is simply assumed to be identical to $F(100\ \mu\text{m})$ because the central wavelength at the C_90 band is 95 μm which is close enough to the IRAS’s 100 μm band. A large error may be associated with the $F(\text{C\_160})$ flux density. For example, combining recent model spectra by Dale et al. (2001) with the same IRAS flux ratio implies $F(\text{C\_160})/F(100\ \mu\text{m})$ = 1.15, leading to a $F(\text{C\_160})$ value greater than the former by ∼25%, which is comparable to the IRAS flux error.

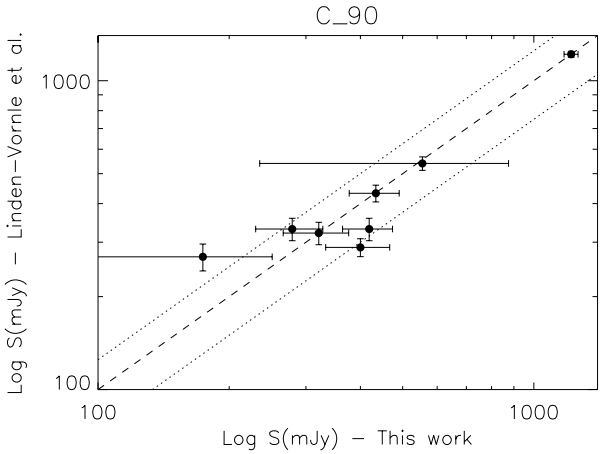

Fig. 2. Comparison with the C_90 flux by Linden-Vørnle et al. The mean ratio of ours to those in Linden-Vørnle et al. are 1.03 and the mean deviation from the line for ratio = 1 (dashed line) is 25% of the flux. The dotted lines denote flux deviations of ±25%. The flux values by Linden-Vørnle et al. are multiplied by a factor of 1.63 so that the C_90 flux of Lockman E4_1 is equal to the IRAS value.

Table 1. Identification with sources in Linden-Vørnle et al.

Linden-Vørnle et al.		This work	
Name	*Flux*(mJy)[a]	Name	*Flux*(mJy)
E1_1	321 ± 27	1EX041	321 ± 55
E1_2	269 ± 27	Note[b]	174 ± 77
E4_1	1218 ± 27	1EX023	1218 ± 45
E4_2	289 ± 19	1EX062	400 ± 67
E4_3	331 ± 28	1EX028/269	419 ± 55
NW1_1	540 ± 27	Note[b]	555 ± 320
NW1_2	331 ± 28	1NW181	279 ± 49
NW2_1	432 ± 27	1NW023/092	434 ± 57

[a] The flux values by Linden-Vørnle et al. are multiplied by a factor of 1.63 so that the C_90 flux of Lockman E4_1 (UGC 06009) is equal to the IRAS value.
[b] These sources are detected by DAOPHOT, but with SNRs < 3.

The following arguments suggest that our flux calibration is associated with a larger source of error than those discussed so far. Our IRAF flux calibration results in 14.4 MJy sr^{-1} at C_90 and 5.17 MJy sr^{-1} at C_160 for the sky background. These are 3.5 times and 1.9 times greater than the COBE values (Paper I). Note that the intensity of interplanetary dust emission varies little with solar elongation at such high ecliptic latitude ($\beta \sim 45°$). The discrepancy can be mostly attributed to the flux loss in the PSF wings and to transients in the detector signals.

The fluxes for IRAS F10507+5723 were determined from the light within the apertures used by the aperture photometry routine PHOT. The radii of the apertures are 69″ for C_90 and 138″ for C_160. The fractions of the PSFs, taken from the calibration files PC1FOOTP.FITS and PC2FOOTP.FITS, passing through the apertures are 0.92 for both C_90 and C_160. Note that the PSFs given in the calibration files agree with the theoretical model PSFs that take into account the ISO primary mirror, secondary mirror, and tripod (Okumura 2000).

The transient effects in the ISOPHOT data have been analyzed and discussed by Acosta-Pulido et al. (1999). When the illumination changes, a generally observed effect in the transients is an instantaneous signal jump followed by a slow rise of the signal until stabilization is reached. The instantaneous signal jumps are ∼0.30 of the stabilized value at C_90 with the C100 detectors and ∼0.85 at C_160 with the C200 detectors. For the C200 detectors, the time constant for the slow rise is ∼40 s (see Fig. 5 in Lagache & Dole 2001). In our 20 s integration, the signal reaches a level of 0.91. Hence, the correction for the transient effect is 0.88 (i.e., average of 0.85 and 0.91) at C_160 for point sources. Note that such a correction should not be applied to the sky background because its spatial distribution is extremely smooth and flat. For the C100 detectors, the time constant is longer than that for the C200 detectors, and it takes several hundreds of seconds to reach stabilization of the signal (see Fig. 7 in Acosta-Pulido et al. 1999). In our 16 s integratio, the signal reaches a level of ∼0.60. Thus, the correction for the transients is roughly ∼0.45 at C_90.

After applying the corrections to the point source for the effects of the PSFs and the transients, the IRAS flux scaling gives sky background values that are 1.45 and 1.55 times greater than the COBE values. Thus, our calibration may overestimate the fluxes by 45% at C_90 and 55% at C_160. Taking all of the errors into account, the total errors associated with our flux calibrations are estimated to be 50% at C_90 and 65% at C_160; i.e., in the case of C_160, a 25% error for the IRAS 100 μm flux, 25% for the model prediction, and 55% for the deviation from the COBE flux.

3.3. Comparison with Linden-Vørnle et al.

Linden-Vørnle et al. (2000) have reduced our C_90 data in the LHEX and LHNW fields by using the PIA with median filtering similar to our image processing. They then used SExtractor to detect and measure sources. Their flux calibration is based on the calibration files supplied with PIA v7.31(e). IRAS F10507+5723 then has a C_90 flux of 747 mJy, which is 1.63 times smaller than the IRAS value. To be consistent with our flux scaling, their C_90 fluxes are multiplied by 1.63 in the following discussion.

They detected 8 sources that are brighter than 269 mJy. In Fig. 1, these sources are marked by a "+" symbol. As can be seen from the maps, these are the brightest sources in our observations. Table 1 identifies their sources with our sources having a $SNR \geq 3$. Two of their eight sources are resolved into two sources, while two are not detected because the SNRs are less than 3. One of the two resolved sources, called E4_3 by Linden-Vørnle et al. (2000), is also resolved into two sources in high spatial resolution VLA observations (De Ruiter et al. 1997), suggesting that DAOPHOT is a useful tool for extracting far-infrared sources in crowded fields. It is also possible that the two undetected sources are extended or that they are multiple sources, where DAOPHOT has failed to fit PSFs with sufficient SNRs.

Figure 2 compares the Linden-Vørnle et al. fluxes with ours. After multiplying by 1.63, the mean ratio of our fluxes to their

fluxes is 1.03 and the mean deviation from the line of ratio = 1 is 25% of the flux, thus being in agreement within 25%. As can be recognized from Table 1 and Fig. 2, their flux errors are approximately two or three times smaller than ours. As will be discussed in Sect. 4.2, our flux error is estimated from the simulations, and thus it includes the confusion noise due to the high source density which is a dominant noise source in our survey observation. On the other hand, Linden-Vørnle et al. (2000) did not perform simulations, thus their flux error does not include such confusion noise. This could explain why their flux errors are two to three times smaller than ours.

4. Simulations and noise

4.1. Simulations

To estimate the errors and bias in detection, photometry, and astrometry, we have carried out simulations using artificial objects. In crowded fields where the detection limits are controlled by the confusion noise, strong Eddington/Malmquist noise is expected. Near the detection limit, more sources are scattered to brighter fluxes (e.g., Oliver 2002). In fact, in crowed fields there is a good chance of having more than one source within a photometric aperture resulting in the two sources being detected as a single brighter source. This results in overestimating the flux (flux bias) and thus the number of bright sources.

It would be ideal to add the signals of artificial sources to the ERD data in such a way that all of the routines used in the data reduction can be checked by the simulations. However, such simulations are very time-consuming and require complete knowledge of such systematic effects as transient behavior of the detectors and incident stray light. However, because of our incomplete understanding of such effects, we decided to perform the simulation by adding artificial objects to the original maps shown in Fig. 1.

Detections and measurements were made on simulation maps, to which artificial objects were added by using the same set of DAOPHOT parameters as used to detect sources in the original maps. The simulations were repeated by changing the positions and fluxes of artificial objects until a statistically sufficient number of objects had been detected. The fluxes given in the simulations range from 50–200 mJy for C_90 and from 70–280 mJy for C_160 in steps of 0.15 dex ($\sqrt{2}\times$). The results from the simulations are summarized in Figs. 3 and 4. The top panels in Fig. 3 indicate the expected flux bias; the ratio of the measured flux over the given flux increases as the given flux decreases. The bottom panels show a rapid slowdown of the growth in source counts toward the faint end of the flux range. In other words, the detection rates rapidly decrease as the flux decreases.

The derived correction factors to the source counts are given in Table 2. The values of the correction factors listed in the table are marked by crosses in Fig. 3. It can reasonably be assumed that sources brighter than 400 mJy are free from the effects of Eddington/Malmquist bias. As one can see from this table and Fig. 3, the corrections for source confusion are important for determining source counts. For example, 30% of the 100–141 mJy C_90 sources are detected as 1.78× brighter sources, while 64% of the 200–283 mJy C_160 sources are detected as 1.31× brighter sources.

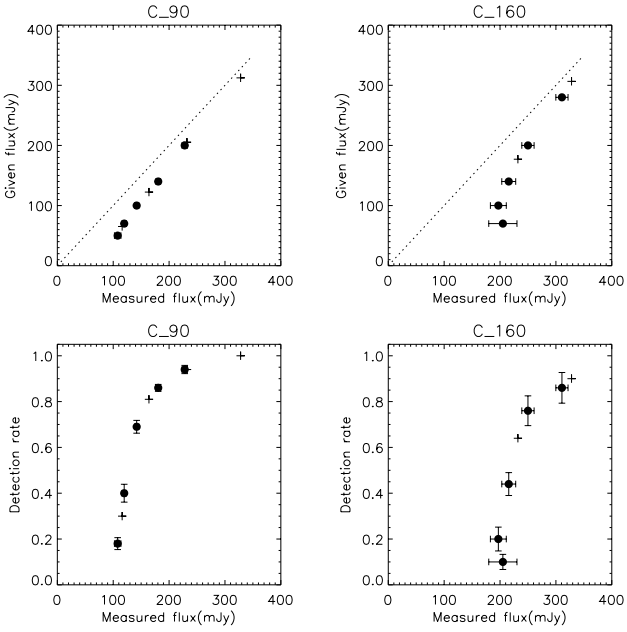

Fig. 3. Summary of the simulations for detection of C_90 (left panels) and C_160 (right panels) sources. The top panels plot the flux given to artificial objects against the flux measured by DAOPHOT. The dotted lines denote the ideal case where the given flux is identical to the measured flux. Due to Eddington/Malmquist bias, the ratio of the measured flux to the given flux increases as the given flux decreases. The bottom panels shows the detection rates as a function of the measured flux. The crosses represent the values of the corrections applied to the source counts (see Table 2).

4.2. Noise

The PIA provides a determination of the signal uncertainty at the individual raster positions. This PIA noise can be used to estimate the instrument noise (Kiss et al. 2001). With PIA Ver8.1, we have produced uncertainty maps. The median filtering technique reduces the PIA noise significantly, namely 2× and 5× smaller than those without this technique at C_90 and C_160, respectively. The typical 1 σ noise levels are 1.3 mJy per $46'' \times 46''$ pixel at C_90 and 0.6 mJy per $92'' \times 92''$ pixel at C_160, after the IRAS-based flux calibration is applied. These values correspond to 3.1 mJy within a PSF-fitting radius of $62''$ at C_90 and 1.4 mJy within a $124''$ radius at C_160. As will be discussed later, the instrumental noise is much smaller than that estimated from the simulations.

The confusion noise due to IR cirrus should not be a dominant noise source given the low level of the total HI column density for our two LH fields. Analyzing the brightness fluctuation at C_90 and C_160 in our fields, Matsuhara et al. (2000) in Paper II found that the spatial power spectrum was flat at low spatial frequencies ($f < 0.1$ arcmin^{-1}) and was slowly decreasing toward higher frequencies. These spectra are quite different from the power-law spectra expected from IR cirrus, and are well explained by randomly distributed sources (i.e.,

Table 2. Corrections for source confusion estimated from simulation.

Flux bin	Flux bias[a]		Detection rate[b]	
(mJy)	C_90	C_160	C_90	C_160
–400	1.00 ± 0.02	1.00 ± 0.04	1.00 ± 0.02	1.00 ± 0.07
400–283	1.05 ± 0.02	1.07 ± 0.04	1.00 ± 0.02	0.90 ± 0.07
283–200	1.13 ± 0.02	1.31 ± 0.07	0.94 ± 0.02	0.64 ± 0.07
200–141	1.34 ± 0.03		0.81 ± 0.03	
141–100	1.78 ± 0.06		0.30 ± 0.04	

[a] Flux bias defined as $S_{\rm measured}/S_{\rm given}$, where $S_{\rm measured}$ and $S_{\rm given}$ are measured and given flux densities in the simulations.
[b] Detection rate defined as $N_{\rm detected}/N_{\rm given}$, where $N_{\rm detected}$ and $N_{\rm given}$ denote detected and given numbers of sources in the simulations.

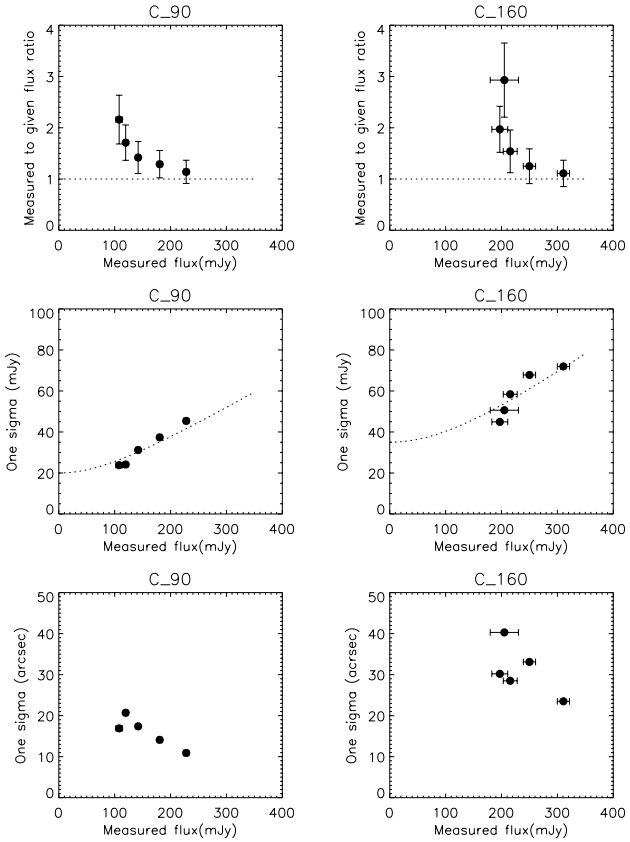

Fig. 4. Accuracy of the catalog data estimated from the simulations for C_90 (left panels) and C_160 (right panels) sources. The top panels show the ratio of the flux measured by DAOPHOT to the flux given to artificial sources. The error bars associated with the flux ratio represent a standard deviation as defined by $\sqrt{\frac{1}{N-1}\sum_{j=0}^{N-1}(x_j-\overline{x})^2}$ where N represents the number of artificial sources detected by DAOPHOT, while the error bars on the measured flux are the standard deviations divided by $\sqrt{N}$. The middle panels show the standard deviations of the measured flux. The dotted lines fitted to the simulation data are given by $\sqrt{\sigma_0^2+\sigma_f^2}$ where σ_0 = constant and $\sigma_f = a \times$ (measured flux): σ_0 = 20 mJy and a = 0.16 for C_90 and σ_0 = 35 mJy and a = 0.20 for C_160. The bottom panels show the standard deviations of the positional differences between measured and given positions.

galaxies). In addition, a point-to-point comparison between C_90 and C_160 brightness shows that the slope of the linear fit is quite different from that expected from IR cirrus (Paper II; Juvela et al. 2000).

Following the technique described by Dole et al. (2001), the total noise including the confusion noise due to the high number density of sources, can be estimated from the results of the simulations. In this technique, the difference between the measured and given fluxes of the artificial objects is regarded as the noise. The middle panels in Fig. 4 show 1 σ dispersions of the differences in flux as a function of the measured flux. The dispersions increase with the fluxes. It is reasonable to approximate the dispersions by a quadratic sum of $\sqrt{\sigma_0^2+\sigma_f^2}$, where σ_0 is constant and σ_f is proportional to the flux (i.e.,$\sigma_f = a \times$ flux). The dotted lines in the figures represent σ_0 = 20 mJy with a = 0.16 for C_90 and σ_0 = 35 mJy with a = 0.2 for C_160. The σ_0 values, corresponding to the noise at zero flux, are much greater than the instrumental noise and the noise due to IR cirrus fluctuations. Thus, we conclude that our observations are limited by the confusion noise due to the high density of galaxies. Our confusion noises are ∼20 mJy at C_90 and ∼35 mJy at C_160. These values are consistent with the value of 45 mJy derived from the C_160 source counts by Dole et al. (2001) and those from the fluctuation analysis of C_90 and C_160 brightness by Kiss et al. (2001).

The standard rule of thumb is that confusion becomes important at 1/30 of a source per beam (Hogg 2001). One sigma confusion noise can be represented as $\sigma^2_{\rm conf}(S_\nu) = -\Omega_{\rm bm}\int_0^{S_\nu} S^2[{\rm d}N(S)/{\rm d}S]{\rm d}S$ by integrating sources fainter than S_ν falling within one beam $\Omega_{\rm bm}$ (e.g., Helou & Beichman 1990; Lagache & Puget 2000) . Assuming the cumulative number counts down to S_ν to be a power law function of the flux density, namely, $N(S_\nu) = KS_\nu^\alpha$, we have $\sigma_{\rm conf}(S_\nu) = [-\alpha/(2+\alpha)\Omega_{\rm bm}N(S_\nu)]^{1/2}S_\nu$. Our cumulative source counts have forms of $N \propto S^{-3.2}$ at C_90 and $N \propto S^{-2.9}$ at C_160. Hence, at the 3 σ limit, namely $S_\nu = 3\sigma_{\rm conf}$, the number of sources for $\alpha = -3$ is $\Omega_{\rm bm}N(S_\nu) = 1/27$. In our source counts, the number of sources brighter than the 3 σ_0 noise levels are 1.5×10^6 and 3.5×10^5 per steradian at C_90 and C_160, respectively. Because the beam solid angles are 46″ × 46″ for C_90 and 92″ × 92″ for C_160, the numbers of sources per beam are 1/13 at C_90 and 1/14 at C_160. Our analysis has thus pushed the confusion limited flux levels beyond the classical limit by a factor of two in terms of sources per beam. This may be largely attributed to use of DAOPHOT for source extraction. As already pointed out, DAOPHOT has been developed to do stellar photometry in crowded fields like the cores of globular clusters. In hoping that DAOPHOT would push the confusion limit to a fainter flux level, we decided to use it for source extraction.

Table 3. Cumulative numbers of sources.

Flux	C_90		C_160	
(mJy)	LHEX	LHNW	LHEX	LHNW
400	1	0	2	0
283	3	0	6	2
200	5	8	16	11
141	22	24	35	27
100	81	67	42	28
70	112	97	44	28
50	116	107	44	28
Area (deg^2)[a]	0.452	0.452	0.443	0.442

[a] Survey areas observed at the specified band. Note that the common areas that were observed at the both bands are 0.426 deg^2 in LHEX and 0.431 deg^2 in LHNW.

5. Catalogs, positional accuracy, and IR colors

5.1. Separate catalogs for C_90 and C_160 sources

To construct the ISO far-infrared catalogs that will be used in the subsequent analysis, we have selected sources with $SNR > 3$, excluding areas near the edges of the maps. The redundancy of the observations along the edges of the maps is less than for the inner regions, implying poorer sensitivity near the edges. The widths of these edges correspond to the size of the detector, namely 46″ at C_90 and 92″ at C_160. As given in Table 3, the total survey areas are 0.904 deg^2 at C_90 and 0.885 deg^2 at C_160. C_90 and C_160 observations were not performed in the same revolution so that each has a different roll angle, resulting in some small areas where observations were only performed at a single band. The common areas in which both C_90 and C_160 observations were made are 0.426 deg^2 for LHEX and 0.431 deg^2 for LHNW. The total common area is thus 0.857 deg^2, which is 95% of the total area observed at C_90 and 97% at C_160.

The catalogs are given in Tables 4–7. As summarized in Table 3, the numbers of sources listed in the catalogs are 223 at C_90 and 72 at C_160; thus there are 295 entries in total. The first column of the catalogs gives the names of sources. C_90 and C_160 sources in LHEX are prefixed 1EX and 2EX, respectively, and those in LHNW are prefixed 1NW and 2NW, respectively. The three digits following the prefix are running numbers given by DAOPHOT. Therefore, 2NW007 means the 7th source in LHNW detected in the C_160 band. Columns 2 and 3 give the right ascension and declination (J2000). The errors in position estimated from the simulations are given in the bottom panels of Fig. 4. They are estimated to be 20″ at C_90 and 35″ at C_160. As will be discussed in the next subsection, these errors are consistent with those estimated from Fig. 5. Column 4 shows the flux density in mJy along with the error. Column 5 gives the SNR estimated from DAOPHOT photometry. The flux errors for sources fainter than 400 mJy are estimated from the simulations as shown in the middle panels of Fig. 4. For brighter sources, the flux errors are simply the flux divided by the SNR. No correction for flux bias was applied to the flux density values given in the catalogs. Notes are given in Col. 6. The area observed at C_90 differs slightly from that at C_160 due to field rotation; therefore some sources were only observed at either C_90 or C_160. Such sources are marked “*” in the last column.

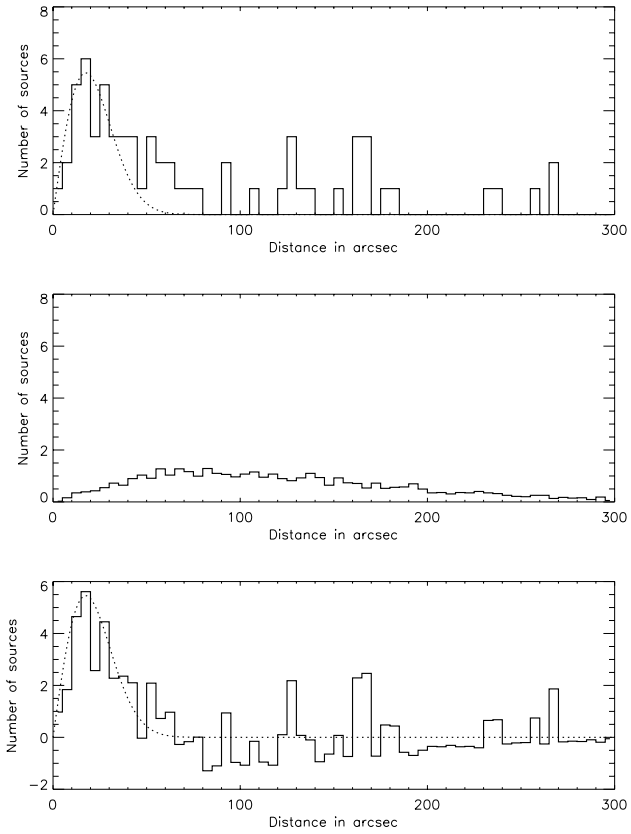

Fig. 5. The distributions of associations between C_160 and C_90 sources as a function of distance, where distance is an angular separation from a C_160 source to the nearest C_90 source. The top panel shows the observed 65 associations with a distance of 300″ or less. The middle panel represents background associations expected from uniformly-distributed, random positions of sources. The bottom panel shows the difference between the observed and background associations, thus presumably real associations only plus statistical fluctuation. The dotted curve in the top and bottom panels represents the distributions for the case that all associations are physically real and the positional errors are identical to those estimated by the simulations (i.e., $\sigma_{C\_160} = 35''$ and $\sigma_{C\_90} = 20''$). In the top panel, 84% of the observed association with distances less than 50″ are expected to be real.

5.2. Cross-association catalogs of C_90 and C_160 sources

To merge the separate catalogs, C_160 sources were cross-associated with C_90 sources. To do this, C_160 sources were coupled to the nearest C_90 source and their angular separations were computed. This was done for 70 C_160 sources that were all “detected” at C_90. The results are given in the top panel of Fig. 5. The distribution of the observed associations consist of real physical associations and fault background associations that are produced by chance. To estimate the number of background associations, we generated C_90 and C_160 sources at positions which are distributed

Table 4. C_90 (90 μm) sources in LHEX.

Name	RA (J2000)	Dec (J2000)	Flux (mJy)	SNR	Note
1EX182	10 49 27.0	57 06 46	72.9 ± 23.2	3.4	*
1EX180	10 49 37.1	57 17 50	107.8 ± 26.4	3.4	
1EX200	10 49 40.2	57 07 59	159.4 ± 32.4	3.4	
1EX118	10 49 42.6	57 05 43	123.3 ± 28.1	3.9	
1EX279	10 49 45.8	57 16 50	131.7 ± 29.1	3.9	
1EX164	10 49 46.8	57 14 57	126.1 ± 28.4	3.9	
1EX136	10 49 48.0	57 23 17	122.0 ± 27.9	4.5	
1EX096	10 49 53.6	57 37 35	131.8 ± 29.1	3.9	
1EX166	10 49 55.0	57 32 26	116.6 ± 27.4	4.5	
1EX093	10 49 56.2	57 18 05	135.4 ± 29.5	5.4	
1EX261	10 49 57.3	57 04 43	94.0 ± 25.0	6.8	
1EX305	10 49 57.8	57 14 40	115.4 ± 27.2	3.9	
1EX175	10 50 01.1	57 09 32	138.2 ± 29.8	5.4	
1EX165	10 50 01.2	57 21 48	114.4 ± 27.1	6.8	
1EX408	10 50 01.9	57 03 13	105.7 ± 26.2	3.4	
1EX385	10 50 01.9	57 36 33	83.2 ± 24.0	3.9	
1EX133	10 50 03.7	57 08 09	135.7 ± 29.5	9.0	
1EX153	10 50 03.7	57 16 24	109.8 ± 26.6	3.4	
1EX313	10 50 08.8	57 35 47	85.0 ± 24.2	3.9	
1EX197	10 50 08.8	57 06 29	183.3 ± 35.5	5.4	
1EX294	10 50 11.5	57 04 52	132.8 ± 29.2	3.9	
1EX116	10 50 12.3	57 12 10	150.8 ± 31.3	9.0	
1EX333	10 50 14.6	57 43 07	83.0 ± 24.0	3.0	*
1EX039	10 50 14.7	57 09 49	90.0 ± 24.6	3.0	
1EX117	10 50 18.0	57 28 06	117.9 ± 27.5	5.4	
1EX094	10 50 18.9	57 36 03	106.2 ± 26.2	3.4	
1EX284	10 50 18.9	57 04 19	132.6 ± 29.2	4.5	
1EX091	10 50 19.5	57 24 53	103.9 ± 26.0	3.9	
1EX204	10 50 20.2	57 05 27	79.6 ± 23.7	3.0	
1EX190	10 50 21.4	57 42 03	104.1 ± 26.0	5.4	*
1EX143	10 50 27.9	57 20 20	131.4 ± 29.0	4.5	
1EX193	10 50 31.4	57 04 33	115.8 ± 27.3	3.9	
1EX251	10 50 34.8	57 07 35	102.1 ± 25.8	5.4	
1EX088	10 50 37.9	57 28 53	148.5 ± 31.1	4.5	
1EX090	10 50 39.5	57 41 59	112.0 ± 26.9	3.9	*
1EX048	10 50 42.9	57 06 56	273.4 ± 48.1	13.6	
1EX123	10 50 43.8	57 11 09	97.7 ± 25.4	3.0	
1EX040	10 50 47.7	57 23 24	155.6 ± 31.9	4.5	
1EX086	10 50 50.1	57 32 20	92.4 ± 24.9	3.0	
1EX422	10 50 50.5	57 04 45	104.3 ± 26.0	3.9	
1EX041	10 50 51.6	57 35 14	321.3 ± 55.2	3.9	
1EX260	10 50 54.7	57 03 05	56.8 ± 22.0	3.9	
1EX085	10 50 54.9	57 16 29	123.4 ± 28.1	3.0	
1EX083	10 50 56.3	57 13 21	143.5 ± 30.4	6.8	
1EX084	10 50 59.8	57 20 21	157.2 ± 32.1	5.4	
1EX152	10 51 01.7	57 09 32	115.8 ± 27.3	4.5	
1EX081	10 51 12.9	57 14 24	136.2 ± 29.6	5.4	
1EX038	10 51 17.5	57 28 01	100.1 ± 25.6	3.4	
1EX076	10 51 26.2	57 35 12	188.0 ± 36.1	9.0	
1EX271	10 51 27.3	57 02 27	111.1 ± 26.8	4.5	
1EX075	10 51 31.9	57 34 02	108.1 ± 26.4	3.0	
1EX100	10 51 32.8	57 29 39	108.7 ± 26.5	3.9	
1EX101	10 51 36.8	57 42 04	129.9 ± 28.8	5.4	*
1EX036	10 51 37.8	57 15 02	121.8 ± 27.9	3.4	
1EX037	10 51 41.5	57 21 48	83.0 ± 24.0	3.0	

Columns - Col. 1 Name coded by 1EXnnn where nnn was given by DAOPHOT. Column 5 Signal to Noise Ratio. Column 6 “*” means that no C_160 observations were made for that source, otherwise both C_90 and C_160 observations were performed.

Table 4. continued.

Name	RA (J2000)	Dec (J2000)	Flux (mJy)	SNR	Note
1EX202	10 51 43.3	57 28 13	98.1 ± 25.4	3.0	
1EX078	10 51 47.2	57 38 48	108.5 ± 26.5	3.4	
1EX047	10 51 51.6	57 09 28	156.3 ± 32.0	5.4	
1EX072	10 52 03.5	57 40 56	143.2 ± 30.4	5.4	
1EX034	10 52 06.3	57 07 46	165.2 ± 33.1	6.8	
1EX046	10 52 10.8	57 25 29	83.9 ± 24.1	3.0	
1EX070	10 52 19.0	57 41 35	120.8 ± 27.8	3.0	*
1EX148	10 52 25.3	57 02 00	155.3 ± 31.9	3.9	
1EX032	10 52 26.2	57 14 00	94.3 ± 25.1	4.5	
1EX245	10 52 28.9	57 25 41	113.6 ± 27.0	3.0	
1EX130	10 52 31.4	57 09 43	108.2 ± 26.5	4.5	
1EX030	10 52 39.0	57 24 32	171.7 ± 34.0	4.5	
1EX028	10 52 49.1	57 07 43	186.2 ± 35.9	4.5	
1EX303	10 52 52.5	57 29 39	75.1 ± 23.3	5.4	
1EX269	10 52 54.2	57 08 20	232.7 ± 42.3	3.9	
1EX396	10 52 56.5	57 11 28	71.2 ± 23.0	3.9	
1EX045	10 52 57.4	57 28 09	102.8 ± 25.9	3.9	
1EX062	10 53 01.3	57 05 46	399.6 ± 67.0	13.6	
1EX029	10 53 03.0	57 37 07	102.7 ± 25.9	3.4	
1EX316	10 53 03.5	57 12 45	101.2 ± 25.7	3.9	
1EX027	10 53 16.5	57 19 25	107.0 ± 26.3	3.9	
1EX179	10 53 19.8	57 21 39	169.2 ± 33.7	4.5	
1EX126	10 53 22.3	57 15 02	124.4 ± 28.2	4.5	
1EX024	10 53 23.8	57 02 55	103.7 ± 26.0	9.0	
1EX026	10 53 26.1	57 29 06	137.7 ± 29.8	4.5	
1EX346	10 53 26.4	57 00 26	63.5 ± 22.4	3.4	*
1EX025	10 53 27.3	57 11 24	118.6 ± 27.6	4.5	
1EX125	10 53 27.6	57 13 52	132.1 ± 29.1	6.8	
1EX113	10 53 29.6	57 39 21	110.2 ± 26.7	4.5	
1EX056	10 53 32.7	56 59 47	109.6 ± 26.6	3.4	*
1EX315	10 53 33.5	57 36 36	133.7 ± 29.3	4.5	
1EX403	10 53 33.6	57 01 38	68.4 ± 22.8	5.4	
1EX112	10 53 40.5	57 30 38	124.9 ± 28.3	3.0	
1EX060	10 53 41.0	57 25 00	152.1 ± 31.5	5.4	
1EX043	10 53 43.7	57 27 48	130.5 ± 28.9	4.5	
1EX058	10 53 45.8	57 17 41	103.1 ± 25.9	3.0	
1EX139	10 53 47.5	57 38 10	70.2 ± 22.9	3.4	
1EX023	10 53 48.5	57 07 10	1218.0 ± 44.9	27.1	
1EX003	10 53 49.0	57 00 54	79.2 ± 23.7	3.4	*
1EX409	10 53 53.4	57 29 50	106.6 ± 26.3	3.9	
1EX055	10 53 56.4	57 23 32	113.8 ± 27.0	3.0	
1EX161	10 53 58.4	57 27 36	79.2 ± 23.7	4.5	
1EX311	10 53 59.2	57 14 45	84.7 ± 24.2	4.5	
1EX471	10 54 00.6	57 25 54	91.8 ± 24.8	3.9	
1EX053	10 54 01.7	57 20 48	116.1 ± 27.3	5.4	
1EX469	10 54 02.6	57 10 20	71.8 ± 23.1	3.0	
1EX242	10 54 05.7	57 01 58	84.0 ± 24.1	3.4	
1EX224	10 54 05.8	57 08 46	110.7 ± 26.7	5.4	
1EX014	10 54 10.3	57 33 36	99.6 ± 25.6	3.9	
1EX187	10 54 10.6	57 07 32	53.9 ± 21.8	3.9	
1EX410	10 54 14.4	57 35 37	71.3 ± 23.0	3.9	
1EX110	10 54 15.6	57 37 54	76.7 ± 23.5	6.8	
1EX319	10 54 16.9	57 32 40	95.0 ± 25.1	4.5	
1EX107	10 54 16.9	57 22 37	109.1 ± 26.5	4.5	
1EX111	10 54 17.0	57 30 00	108.1 ± 26.4	3.9	
1EX109	10 54 21.9	57 36 47	143.9 ± 30.5	4.5	
1EX201	10 54 26.1	57 27 01	71.0 ± 23.0	4.5	
1EX338	10 54 30.8	57 28 01	76.5 ± 23.4	4.5	*
1EX389	10 54 31.4	57 22 34	89.2 ± 24.6	3.4	*
1EX011	10 54 32.1	57 32 53	78.9 ± 23.7	3.9	*
1EX178	10 54 34.5	57 29 11	83.6 ± 24.1	5.4	*

Table 5. C_90 (90 μm) sources in LHNW.

Name	RA (J2000)	Dec (J2000)	Flux (mJy)	SNR	Note
1NW078	10 31 01.7	57 35 08	109.1 ± 26.5	3.0	*
1NW434	10 31 22.8	57 45 46	106.5 ± 26.3	3.0	
1NW130	10 31 23.1	57 42 36	204.2 ± 38.3	9.0	
1NW109	10 31 27.4	57 32 43	107.5 ± 26.4	3.9	
1NW442	10 31 28.2	57 37 35	103.4 ± 26.0	3.0	
1NW468	10 31 28.6	57 40 46	98.5 ± 25.5	3.4	
1NW183	10 31 29.7	57 44 32	140.0 ± 30.0	9.0	
1NW262	10 31 43.8	57 57 02	88.1 ± 24.5	4.5	
1NW034	10 31 47.0	57 49 50	161.2 ± 32.6	5.4	
1NW076	10 31 47.6	57 55 59	119.6 ± 27.7	5.4	
1NW448	10 31 51.4	57 47 38	88.1 ± 24.5	3.4	
1NW282	10 31 52.0	57 58 22	79.2 ± 23.7	3.0	
1NW387	10 31 53.0	58 01 11	145.4 ± 30.7	6.8	
1NW118	10 31 56.3	57 56 51	148.3 ± 31.0	4.5	
1NW107	10 31 59.3	57 44 08	102.2 ± 25.8	3.4	
1NW305	10 32 00.9	57 59 50	56.2 ± 21.9	6.8	
1NW169	10 32 02.2	57 55 42	127.7 ± 28.6	3.4	
1NW181	10 32 02.9	58 07 59	278.8 ± 48.9	3.0	
1NW077	10 32 05.9	58 02 47	163.1 ± 32.9	5.4	
1NW246	10 32 06.0	57 45 35	89.0 ± 24.6	4.5	
1NW165	10 32 09.4	57 59 14	120.5 ± 27.8	6.8	
1NW311	10 32 09.7	58 01 42	94.6 ± 25.1	3.9	
1NW239	10 32 11.1	57 32 34	145.6 ± 30.7	3.9	
1NW171	10 32 12.4	58 09 31	87.7 ± 24.4	4.5	*
1NW261	10 32 13.0	57 58 05	103.5 ± 26.0	3.0	
1NW385	10 32 13.3	58 06 31	105.0 ± 26.1	5.4	
1NW172	10 32 15.6	57 30 46	70.0 ± 22.9	3.4	
1NW146	10 32 22.0	57 59 56	153.1 ± 31.6	3.9	
1NW147	10 32 24.0	58 03 20	120.8 ± 27.8	3.0	
1NW297	10 32 28.6	58 07 22	117.0 ± 27.4	4.5	
1NW245	10 32 31.6	57 35 13	71.1 ± 23.0	3.0	
1NW145	10 32 34.0	58 00 00	115.8 ± 27.3	4.5	
1NW193	10 32 40.0	57 36 05	107.0 ± 26.3	9.0	
1NW143	10 32 45.0	57 47 20	64.2 ± 22.5	3.4	
1NW260	10 32 45.5	58 01 00	140.6 ± 30.1	5.4	
1NW192	10 32 49.0	57 37 00	249.4 ± 44.6	6.8	
1NW032	10 32 50.9	57 33 28	200.7 ± 37.8	9.0	
1NW070	10 32 53.5	58 06 25	212.6 ± 39.5	6.8	
1NW102	10 32 57.5	57 31 11	149.6 ± 31.2	13.6	
1NW116	10 33 04.8	57 42 43	43.9 ± 21.2	3.0	
1NW190	10 33 10.5	57 29 42	81.9 ± 23.9	3.9	
1NW256	10 33 12.2	57 33 12	128.1 ± 28.6	3.9	
1NW031	10 33 14.7	57 31 35	168.4 ± 33.6	4.5	
1NW236	10 33 17.3	57 28 38	69.9 ± 22.9	3.0	
1NW066	10 33 17.6	58 05 22	120.2 ± 27.7	4.5	
1NW021	10 33 19.5	57 49 22	167.1 ± 33.4	5.4	
1NW380	10 33 20.5	57 27 21	56.2 ± 21.9	3.0	
1NW114	10 33 25.2	57 45 40	104.6 ± 26.1	3.0	
1NW060	10 33 26.5	57 38 08	107.3 ± 26.4	4.5	
1NW062	10 33 28.8	57 42 16	110.8 ± 26.7	3.9	
1NW142	10 33 33.0	58 05 19	121.5 ± 27.9	3.0	
1NW185	10 33 35.0	57 32 35	145.9 ± 30.7	5.4	
1NW115	10 33 35.2	57 55 40	121.9 ± 27.9	4.5	
1NW177	10 33 35.7	57 30 30	98.4 ± 25.5	3.0	
1NW103	10 33 41.2	58 07 28	162.5 ± 32.8	5.4	

Note – Same as Table 4, but with name 1NWnnn for LHNW.

Table 5. continued.

Name	RA (J2000)	Dec (J2000)	Flux (mJy)	SNR	Note
1NW357	10 33 42.0	57 27 21	97.9 ± 25.4	3.9	
1NW195	10 33 49.8	58 05 37	102.0 ± 25.8	3.9	
1NW152	10 33 51.3	57 29 49	116.5 ± 27.3	5.4	
1NW241	10 33 51.6	57 31 02	88.5 ± 24.5	3.9	
1NW100	10 33 53.3	57 27 19	114.8 ± 27.2	6.8	
1NW030	10 33 58.0	57 43 26	149.4 ± 31.2	5.4	
1NW272	10 33 59.2	57 29 37	138.6 ± 29.9	4.5	
1NW309	10 33 59.6	57 26 23	56.9 ± 22.0	3.0	
1NW395	10 34 00.8	58 03 50	115.0 ± 27.2	4.5	
1NW020	10 34 03.8	57 51 26	99.9 ± 25.6	3.9	
1NW300	10 34 08.6	57 28 23	90.0 ± 24.6	3.9	
1NW221	10 34 09.6	57 27 04	112.2 ± 26.9	5.4	
1NW441	10 34 10.4	58 03 59	89.1 ± 24.6	3.0	
1NW170	10 34 10.4	58 01 03	124.6 ± 28.2	4.5	
1NW088	10 34 10.9	57 44 57	114.5 ± 27.1	4.5	
1NW382	10 34 14.6	58 06 19	93.9 ± 25.0	3.0	
1NW112	10 34 19.6	57 24 49	108.0 ± 26.4	3.4	*
1NW086	10 34 19.7	57 47 31	84.2 ± 24.1	3.9	
1NW313	10 34 20.5	58 05 10	64.8 ± 22.5	3.0	*
1NW373	10 34 29.5	57 25 01	85.8 ± 24.3	3.4	
1NW057	10 34 32.3	57 54 14	99.3 ± 25.5	4.5	
1NW111	10 34 47.2	57 25 13	92.7 ± 24.9	3.4	
1NW027	10 34 52.6	57 50 30	94.6 ± 25.1	3.0	
1NW445	10 34 58.0	57 58 55	129.3 ± 28.8	3.4	
1NW094	10 34 58.7	57 26 31	79.9 ± 23.7	3.0	
1NW084	10 35 01.2	57 59 50	100.5 ± 25.7	3.4	
1NW049	10 35 01.6	57 30 20	103.7 ± 26.0	3.9	
1NW134	10 35 07.9	58 01 51	91.2 ± 24.8	3.0	
1NW056	10 35 09.3	57 56 12	98.1 ± 25.4	3.0	
1NW037	10 35 12.7	57 48 01	97.4 ± 25.4	3.0	
1NW026	10 35 13.9	57 34 53	106.4 ± 26.3	3.9	
1NW247	10 35 15.9	57 44 02	107.2 ± 26.3	3.4	
1NW025	10 35 16.2	57 33 19	137.9 ± 29.8	4.5	
1NW055	10 35 19.7	58 00 53	147.7 ± 31.0	5.4	
1NW093	10 35 21.1	57 30 07	114.2 ± 27.1	4.5	
1NW051	10 35 26.4	57 45 07	107.5 ± 26.4	3.9	
1NW217	10 35 31.3	57 24 21	91.0 ± 24.7	5.4	
1NW043	10 35 32.6	57 31 37	128.4 ± 28.7	4.5	
1NW052	10 35 44.9	57 59 14	146.8 ± 30.8	3.9	
1NW189	10 35 51.4	57 51 48	119.7 ± 27.7	3.4	
1NW082	10 35 59.2	57 37 43	84.3 ± 24.1	3.0	
1NW042	10 36 01.9	57 34 50	41.4 ± 21.1	3.0	
1NW092	10 36 03.2	57 48 30	231.7 ± 42.1	5.4	
1NW023	10 36 05.0	57 47 21	202.3 ± 38.0	5.4	
1NW022	10 36 11.9	57 43 20	146.0 ± 30.8	4.5	
1NW045	10 36 12.4	57 56 56	95.5 ± 25.2	3.4	
1NW133	10 36 14.0	57 39 08	202.3 ± 38.0	4.5	
1NW200	10 36 25.3	57 50 10	66.6 ± 22.7	4.5	
1NW201	10 36 36.3	57 52 44	65.2 ± 22.6	3.0	
1NW148	10 36 37.8	57 58 52	104.7 ± 26.1	3.9	
1NW126	10 36 43.5	57 53 27	74.9 ± 23.3	5.4	*
1NW178	10 36 47.7	57 59 34	154.2 ± 31.8	3.9	*

Table 6. C_160 (170 μm) sources in LHEX.

Name	RA (J2000)	Dec (J2000)	Flux (mJy)	SNR	Note
2EX028	10 49 32.0	57 19 13	132.3 ± 43.9	3.4	
2EX032	10 49 35.0	57 06 20	101.9 ± 40.5	3.9	
2EX066	10 49 40.2	57 34 27	161.2 ± 47.6	5.4	*
2EX027	10 49 48.6	57 17 14	248.1 ± 60.7	5.4	
2EX031	10 49 51.7	57 34 51	343.1 ± 77.0	5.4	
2EX035	10 49 58.4	57 40 15	159.5 ± 47.4	3.4	
2EX108	10 50 02.0	57 14 28	177.9 ± 49.9	3.9	
2EX026	10 50 11.6	57 28 12	91.5 ± 39.5	3.0	
2EX061	10 50 16.6	57 12 29	165.9 ± 48.2	3.4	
2EX025	10 50 37.6	57 28 52	149.4 ± 46.0	3.9	
2EX095	10 50 39.7	57 16 37	156.1 ± 46.9	4.5	
2EX004	10 50 43.9	57 07 01	407.6 ± 30.0	13.6	
2EX013	10 50 49.7	57 35 07	353.0 ± 78.8	3.9	
2EX068	10 50 55.5	57 15 57	211.4 ± 54.9	9.0	
2EX024	10 51 01.9	57 41 24	224.0 ± 56.9	3.9	
2EX115	10 51 18.3	57 14 31	259.6 ± 62.6	4.5	
2EX060	10 51 18.5	57 35 26	177.9 ± 49.9	5.4	
2EX110	10 51 18.7	57 19 11	154.4 ± 46.7	4.5	
2EX012	10 51 21.0	57 16 33	128.5 ± 43.4	4.5	
2EX041	10 51 32.0	57 40 53	238.7 ± 59.2	3.0	
2EX057	10 51 42.4	57 21 27	120.0 ± 42.4	3.0	
2EX034	10 51 43.8	57 29 17	160.2 ± 47.5	4.5	
2EX040	10 51 46.4	57 38 46	262.4 ± 63.1	6.8	
2EX036	10 51 49.4	57 09 22	285.9 ± 67.0	5.4	
2EX016	10 52 03.3	57 07 44	242.9 ± 59.9	6.8	
2EX120	10 52 11.6	57 03 21	148.3 ± 45.9	3.4	
2EX111	10 52 12.3	57 39 08	157.7 ± 47.1	3.4	
2EX103	10 52 25.4	57 01 32	301.6 ± 69.7	5.4	
2EX059	10 52 29.2	57 09 13	143.3 ± 45.2	4.5	
2EX015	10 52 33.9	57 31 18	224.8 ± 57.0	3.9	
2EX050	10 52 47.6	57 36 08	190.1 ± 51.7	4.5	
2EX047	10 52 56.1	57 07 56	230.9 ± 57.9	3.9	
2EX056	10 53 01.0	57 15 24	118.6 ± 42.3	3.9	
2EX044	10 53 03.3	57 05 33	150.6 ± 46.2	3.4	
2EX010	10 53 06.4	57 34 03	233.9 ± 58.4	9.0	
2EX064	10 53 14.5	57 20 04	170.4 ± 48.9	5.4	
2EX083	10 53 19.6	57 37 45	157.0 ± 47.0	3.9	
2EX009	10 53 24.7	57 17 47	182.6 ± 50.6	6.8	
2EX008	10 53 24.9	57 14 03	152.6 ± 46.4	5.4	
2EX021	10 53 47.0	57 07 01	1133.0 ± 83.3	13.6	
2EX045	10 53 57.8	57 32 57	91.5 ± 39.5	3.4	
2EX100	10 54 12.5	57 32 02	120.5 ± 42.5	3.9	
2EX087	10 54 14.1	57 29 57	157.8 ± 47.1	6.8	
2EX046	10 54 27.9	57 28 15	111.7 ± 41.5	3.9	

Columns – Col. 1 Name coded by 2EXnnn where nnn was given by DAOPHOT. Column 5 Signal to Noise Ratio. Column 6 “*” means that no C_90 observations were made for that source, otherwise both C_90 and C_160 observations were performed.

Table 7. C_160 (170 μm) in LHNW.

Name	RA (J2000)	Dec (J2000)	Flux (mJy)	SNR	Note
2NW013	10 31 24.8	57 42 39	366.6 ± 81.2	6.8	
2NW031	10 31 42.5	57 40 04	239.3 ± 59.3	3.4	
2NW016	10 31 54.7	57 56 52	149.4 ± 46.0	3.0	
2NW027	10 32 02.1	58 07 51	272.5 ± 64.8	6.8	
2NW012	10 32 14.5	57 30 14	210.2 ± 54.7	3.9	
2NW011	10 32 25.4	57 52 31	152.4 ± 46.4	3.9	
2NW003	10 32 47.7	57 36 45	292.8 ± 68.2	6.8	
2NW030	10 32 58.6	58 06 18	169.0 ± 48.7	5.4	
2NW005	10 33 18.5	57 49 15	247.9 ± 60.7	3.9	
2NW010	10 33 19.5	58 04 29	168.5 ± 48.6	4.5	
2NW004	10 33 44.5	58 02 13	232.0 ± 58.1	6.8	
2NW040	10 33 46.8	58 07 36	202.4 ± 53.5	5.4	*
2NW009	10 33 59.5	57 29 21	251.8 ± 61.3	6.8	
2NW050	10 33 59.6	58 06 25	136.5 ± 44.4	4.5	
2NW026	10 34 02.3	57 43 16	184.1 ± 50.8	3.0	
2NW008	10 34 52.3	57 41 06	172.1 ± 49.1	5.4	
2NW045	10 34 58.6	57 50 01	182.2 ± 50.5	3.9	
2NW055	10 35 10.3	57 48 15	170.1 ± 48.8	4.5	
2NW039	10 35 15.3	57 53 50	167.3 ± 48.4	5.4	
2NW006	10 35 17.0	57 33 22	228.6 ± 57.6	4.5	
2NW024	10 35 21.2	57 44 38	179.4 ± 50.1	4.5	
2NW007	10 35 24.6	57 51 50	265.8 ± 63.6	6.8	
2NW047	10 35 37.4	57 50 17	171.8 ± 49.0	5.4	
2NW025	10 35 40.9	57 35 44	148.9 ± 46.0	3.9	
2NW023	10 35 51.0	57 43 50	153.5 ± 46.6	3.4	
2NW052	10 35 57.7	57 47 34	149.9 ± 46.1	3.4	
2NW032	10 36 07.0	57 51 35	150.9 ± 46.2	4.5	
2NW022	10 36 13.2	57 43 12	165.4 ± 48.2	4.5	

Note – Same as Table 6, but with name 2NWnnn for LHNW.

at random. The number of sources and the field areas are the same as those where the observations were performed. This operation was repeated 50 times so that a statistically sufficient number of background associations were obtained.

The distribution of background associations are given in the middle panel of Fig. 5. The background is normalized in such a way that the total number of background associations within a distance range (i.e., angular separation) 100–300″ is equal to that of observed associations in the same distance range. The difference between the observed and the background associations, which presumably represents real associations only (plus statistical fluctuation), is given in the bottom panel of Fig. 5. The dotted lines in Fig. 5 show the distribution for the real associations with positional errors of 20″ and 35″ for C_90 and C_160 sources, respectively. These errors are obtained through the simulations. Judging from a comparison between the top panel (observed associations) and the bottom panel (presumably real associations plus statistical fluctuation), 85% of the observed associations with a distance of 50″ or less are real.

The cross-association catalogs are given in Tables 8 and 9. All the associations with a distance of 50″ or less are regarded as real, and listed in the catalogs. Columns 1 and 2 give the names of C_160 and C_90 sources, respectively, followed by right ascension and declination measured at C_160 in Cols. 3 and 4. Columns 5 and 6 show the flux density in mJy along with

Table 8. C_160 (170 μm) sources associated with C_90 (90 μm) sources in LHEX.

Name (C_160)	Name (C_90)	RA (J2000)	Dec (J2000)	Flux (C_160) (mJy)	Flux (C_90) (mJy)	Flux ratio (C_160/C_90)	Distance (arcsec)	SNR (C_160)	SNR (C_90)
2EX027	1EX279	10 49 48.6	57 17 14	248.1 ± 60.7	131.7 ± 29.1	1.8	33	5.4	3.9
2EX108	1EX305	10 50 02.0	57 14 28	177.9 ± 49.9	115.4 ± 27.2	1.5	36	3.9	3.9
2EX061	1EX116	10 50 16.6	57 12 29	165.9 ± 48.2	150.8 ± 31.3	1.1	40	3.4	9.1
2EX025	1EX088	10 50 37.6	57 28 52	149.4 ± 46.0	148.5 ± 31.1	1.0	3	3.9	4.5
2EX004	1EX048	10 50 43.9	57 07 01	407.6 ± 30.0	273.4 ± 48.1	1.4	10	13.6	13.6
2EX013	1EX041	10 50 49.7	57 35 07	353.0 ± 78.8	321.3 ± 55.2	1.1	17	3.9	3.9
2EX068	1EX085	10 50 55.5	57 15 57	211.4 ± 54.9	123.4 ± 28.1	1.7	33	9.1	3.0
2EX115	1EX081	10 51 18.3	57 14 31	259.6 ± 62.6	136.2 ± 29.6	1.9	45	4.5	5.4
2EX057	1EX037	10 51 42.4	57 21 27	120.0 ± 42.4	83.0 ± 24.0	1.4	23	3.0	3.0
2EX040	1EX078	10 51 46.4	57 38 46	262.4 ± 63.1	108.5 ± 26.5	2.4	7	6.8	3.4
2EX036	1EX047	10 51 49.4	57 09 22	285.9 ± 67.0	156.3 ± 32.0	1.8	19	5.4	5.4
2EX016	1EX034	10 52 03.3	57 07 44	242.9 ± 59.9	165.2 ± 33.1	1.4	25	6.8	6.8
2EX103	1EX148	10 52 25.4	57 01 32	301.6 ± 69.7	155.3 ± 31.9	1.9	29	5.4	3.9
2EX059	1EX130	10 52 29.2	57 09 13	143.3 ± 45.2	108.2 ± 26.5	1.3	36	4.5	4.5
2EX047	1EX269	10 52 56.1	57 07 56	230.9 ± 57.9	232.7 ± 42.3	0.9	29	3.9	3.9
2EX044	1EX062	10 53 03.3	57 05 33	150.6 ± 46.2	399.6 ± 67.0	0.3	21	3.4	13.6
2EX064	1EX027	10 53 14.5	57 20 04	170.4 ± 48.9	107.0 ± 26.3	1.5	43	5.4	3.9
2EX008	1EX125	10 53 24.9	57 14 03	152.6 ± 46.4	132.1 ± 29.1	1.1	25	5.4	6.8
2EX021	1EX023	10 53 47.0	57 07 01	1133.0 ± 83.3	1218.0 ± 44.9	0.9	16	13.6	27.1
2EX087	1EX111	10 54 14.1	57 29 57	157.8 ± 47.1	108.1 ± 26.4	1.4	24	6.8	3.9

Columns – Col. 1 C_160 source name. Column 2 C_90 source name. Columns 3–4 C_160 source coordinates in J2000. Column 5 C_160 source flux in mJy. Column 6 C_90 source flux in mJy. Column 7 Flux ratio of C_160 over C_90. Column 8 Distance of C_160 source to the nearest C_90 source. Column 9 Signal to Noise Ratio at C_160. Column 10 Signal to Noise Ratio at C_90.

Table 9. C_160 (170 μm) sources associated with C_90 (90 μm) sources in LHNW.

Name (C_160)	Name (C_90)	RA (J2000)	Dec (J2000)	Flux (C_160) (mJy)	Flux (C_90) (mJy)	Flux ratio (C_160/C_90)	Distance (arcsec)	SNR (C_160)	SNR (C_90)
2NW013	1NW130	10 31 24.8	57 42 39	366.6 ± 81.2	204.2 ± 38.3	1.8	15	6.8	9.1
2NW016	1NW118	10 31 54.7	57 56 52	149.4 ± 46.0	148.3 ± 31.0	1.0	13	3.0	4.5
2NW027	1NW181	10 32 02.1	58 07 51	272.5 ± 64.8	278.8 ± 48.9	0.9	11	6.8	3.0
2NW012	1NW172	10 32 14.5	57 30 14	210.2 ± 54.7	70.0 ± 22.9	3.0	34	3.9	3.4
2NW003	1NW192	10 32 47.7	57 36 45	292.8 ± 68.2	249.4 ± 44.6	1.1	19	6.8	6.8
2NW030	1NW070	10 32 58.6	58 06 18	169.0 ± 48.7	212.6 ± 39.5	0.7	42	5.4	6.8
2NW005	1NW021	10 33 18.5	57 49 15	247.9 ± 60.7	167.1 ± 33.4	1.4	11	3.9	5.4
2NW009	1NW272	10 33 59.5	57 29 21	251.8 ± 61.3	138.6 ± 29.9	1.8	17	6.8	4.5
2NW026	1NW030	10 34 02.3	57 43 16	184.1 ± 50.8	149.4 ± 31.2	1.2	37	3.0	5.4
2NW055	1NW037	10 35 10.3	57 48 15	170.1 ± 48.8	97.4 ± 25.4	1.7	25	4.5	3.0
2NW006	1NW025	10 35 17.0	57 33 22	228.6 ± 57.6	137.9 ± 29.8	1.6	8	4.5	4.5
2NW007	Note$^+$	10 35 24.6	57 51 50	265.8 ± 63.6				6.8	
2NW022	1NW022	10 36 13.2	57 43 12	165.4 ± 48.2	146.0 ± 30.8	1.1	14	4.5	4.5

Note – Same as Table 8, but for LHNW.
Note$^+$ – 2NW007 is associated with an extended C_90 source that DAOPHOT does not detect. Its C_90 flux that was manually measured is 198 ± 37 mJy within a 62″ radius aperture.

the errors. The errors for sources fainter than 400 mJy are estimated from the simulations, while those for brighter sources are simply the flux density divided by the SNR. Column 7 gives the flux density ratio of C_160 over C_90. The distance is given in arcsec in Col. 8. In Cols. 9 and 10, SNRs for C_160 and C_90 are given, respectively.

5.3. IR colors

32 C_160 sources are listed in the cross-association catalogs. The diagrams plotting the F(C_160) flux versus the IR color i.e., the flux ratio F(C_160)/F(C_90) are shown in Fig. 6. The upper panel shows error bars, while error bars are omitted from the bottom panel. The errors shown in the upper panel do not include the errors associated with the flux calibration. As discussed above, the flux calibration errors are estimated to be 50% at C_90 and 65% at C_160. In the diagrams the relative positions of all the data points are fixed to each other, but they can move tanslationally up to 65% in the flux axis and 80% in the color axis. The standard source UGC 06009 for the flux calibration is plotted as a filled circle. As discussed in Sect. 3.2,

Table 10. Source counts without the corrections.

Cumulative counts $N_{\rm obs}$ (sr^{-1})			Differential counts $\Delta N_{\rm obs}/\Delta S_{\rm obs}$ (Jy^{-1}sr^{-1})					
Flux	C_90	C_160	Flux bin			Eff. Flux	C_90	C_160
$S_{\rm obs}$(mJy)			su[a]	–	sl[a]	$S^*_{\rm obs}$(mJy)[b]		
400	3.63×10^3 (1.00)	7.42×10^3 (0.71)		–	400			
283	1.09×10^4 (0.58)	2.97×10^4 (0.35)	400	–	283	328	6.20×10^4 (0.71)	1.90×10^5 (0.41)
200	4.73×10^4 (0.28)	1.00×10^5 (0.19)	283	–	200	232	4.39×10^5 (0.32)	8.51×10^5 (0.23)
141	1.67×10^5 (0.15)	2.30×10^5 (0.13)	200	–	141	164	2.05×10^6 (0.17)	2.22×10^6 (0.17)
100	5.38×10^5 (0.08)	2.60×10^5 (0.12)	141	–	100	116	8.95×10^6 (0.10)	7.16×10^5 (0.35)
70	7.60×10^5 (0.07)	2.67×10^5 (0.12)	100	–	70	82	7.57×10^6 (0.13)	2.53×10^5 (0.71)

– Values in parentheses give errors relative to the preceding values; thus, *abc* (*xyz*) means *abc* ± *abc* ∗ *xyz*.
[a] su = $\sqrt{2}$ sl, where su and sl denote upper and lower values in the respective flux bin.
[b] $S^*_{\rm obs}$, effective flux density defined as $S^*_{\rm obs} = \int_{sl}^{su} S\,({\rm d}N/{\rm d}S){\rm d}S \,/\, \int_{sl}^{su} ({\rm d}N/{\rm d}S){\rm d}S$, where $N(S)$ is the cumulative source counts for S or brighter. $S^*_{\rm obs} = 1.16sl$ for $N \propto S^{-3}$, while $S^*_{\rm obs} = 1.20sl$ for ${\rm d}N/{\rm d}S$ = constant. $S^*_{\rm obs} = 1.16sl$ is used in this work, because our counts can be approximated by $N \propto S^{-3.2}$ at C_90 and $N \propto S^{-2.9}$ at C_160.

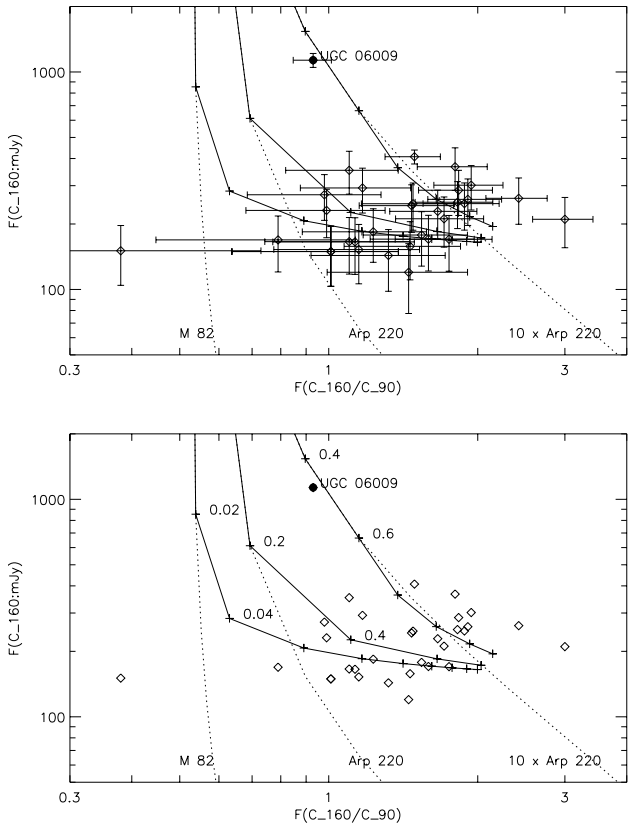

Fig. 6. The C_160 flux plotted versus the ratio of the C_160 flux to the C_90 flux. The upper panel shows error bars, while the error bars are omitted in the bottom panel. The solid lines are predictions for the flux-color relations at various redshifts for M 82, Arp 220, and 10 × Arp 220. The numbers given just to the right of the crosses are redshifts; z = ..., 0.02, 0.04, 0.06, ... for M 82, z = ..., 0.2, 0.4, 0.6, ... for Arp 220, and so on. Flux bias makes the flux brighter and the color redder. The dotted lines represent the flux-color relations without the effect of the flux bias. UGC 06009 is the standard source used for the flux calibration.

UGC 06009 is likely to be a cirrus dominated Sb galaxy and is expected to have a red F(C_160)/F(C_90) color. Nonetheless, most of our sources are redder than UGC 06009. There are three possible reasons making the color red. These are reddening due to flux bias, K-correction brightening (in particular at C_160 due to reshift), and the presence of very cold dust.

To examine the first two causes, the flux-color relations for starburst galaxy M 82, ultra-luminous IR galaxy Arp 220, and 10 × Arp 220 at various redshifts are overlaid in the panels by the solid and dotted lines. These relations are calculated based on the SEDs of M 82 (Efstathiou et al. 2000 and references therein), and the ultra-luminous IR galaxy Arp 220 (Rigopoulou et al. 1996; Klaas et al. 1997). The solid lines include the effect of the flux bias given in the upper panels of Fig. 3 and Table 2, while the dotted lines represent the case without this effect. The flux bias makes the flux brighter and the color redder, and the effect becomes more significant as the flux decreases. The figures imply that a significant fraction of faint sources below 200 mJy at C_160 are starburst galaxies like M 82 and their intrinsic blue colors are reddened by the flux bias. On the other hand, bright sources above 200 mJy with a red color could be dominated by very luminous galaxies such as Arp 220 at moderate redshifts. In addition, there may be a contribution from galaxies having very cold dust (Alton et al. 1998; Haas et al. 1998). The large errors associated with the flux calibration hampers further insight into the flux-color diagrams. Precise measurements of the far-infrared flux for our calibration source UGC 06009 (IRAS F10507+5723) are required from future missions like SIRTF and ASTRO-F.

6. Source counts

The cumulative and differential source counts are tabulated in Table 10. These are “raw” counts derived from Table 3 without any corrections. To obtain “true” counts, the corrections for flux bias and the detection rate should be applied to the un-corrected counts. This is done by using the correction factors tabulated in Table 2, and the resultant corrected counts are given in Table 11. The corrected counts, both in differential and cumulative forms, are compared with the un-corrected counts in Fig. 7. The differential counts are plotted in the top panels, and the cumulative counts in the bottom panels. The data connected by solid lines are corrected counts and those

Table 11. Source counts after corrections for the detection rate and flux bias.

Cumulative counts, N_c (sr^{-1})				Differential counts, $\Delta N_c/\Delta S_c$ (Jy^{-1} sr^{-1})			
C_90		C_160		C_90		C_160	
S_c(mJy)[a]	N_c[b]	S_c(mJy)	N_c	S_c(mJy)[c]	$\Delta N_c/\Delta S_c$[d]	S_c(mJy)	$\Delta N_c/\Delta S_c$
400 (0.02)	3.63×10^3 (1.00)	400 (0.04)	7.42×10^3 (0.71)				
269 (0.02)	1.09×10^4 (0.58)	264 (0.04)	3.22×10^4 (0.36)	313 (0.02)	6.51×10^4 (0.71)	307 (0.04)	2.26×10^5 (0.42)
177 (0.03)	4.96×10^4 (0.28)	153 (0.05)	1.42×10^5 (0.22)	205 (0.03)	5.27×10^5 (0.32)	177 (0.05)	1.74×10^6 (0.26)
106 (0.03)	1.98×10^5 (0.15)			122 (0.03)	3.39×10^6 (0.18)		
56 (0.03)	1.43×10^6 (0.13)			65 (0.03)	5.31×10^7 (0.15)		

[–] Values in parentheses give errors relative to the preceding values; thus, abc (*xyz*) means $abc \pm abc * xyz$.
[a] S_c for cumulative counts is S_{obs} divided by the flux bias.
[b] N_c is the cumulative counts after the correction applied.
[c] S_c for cumulative counts is S^*_{obs} divided by the flux bias.
[d] $\Delta N_c/\Delta S_c$ is the differential counts after the correction has been applied.

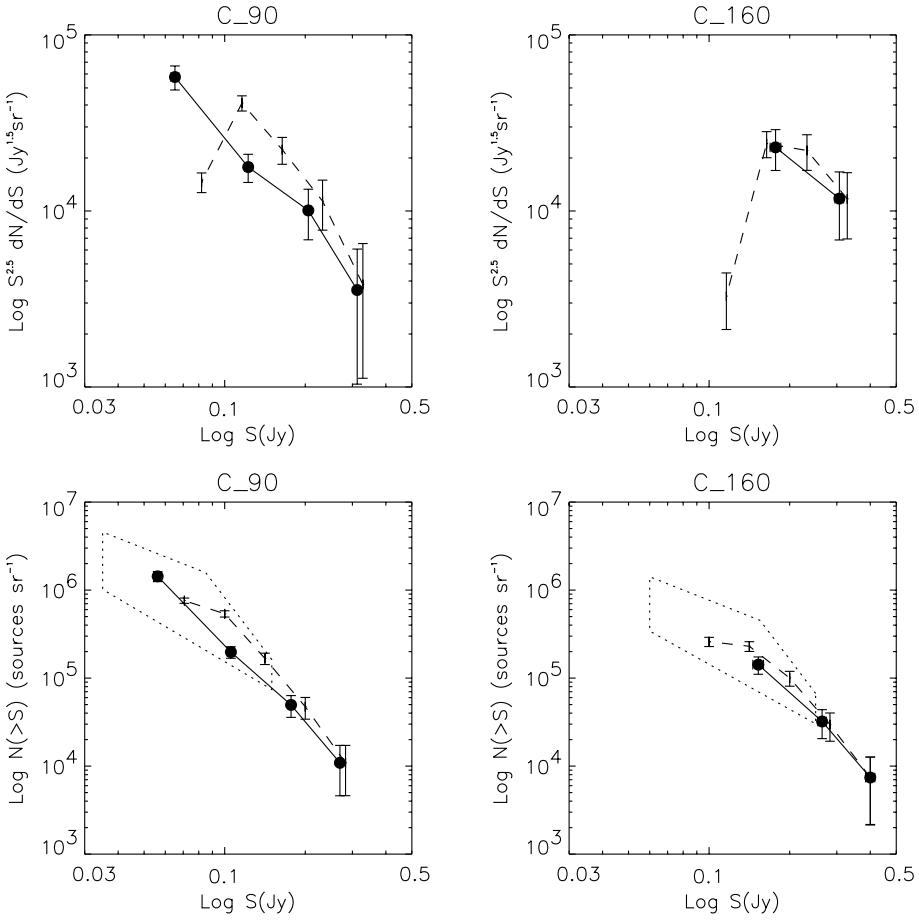

Fig. 7. The source count versus flux-density relations plotted for ISO far-infrared sources in the Lockman Hole. The top panels show differential counts for C_90 sources on the left and C_160 sources on the right. The data connected by the dashed line are those without the corrections. The vertical error bars shown are statistical errors only i.e., $\sqrt{N}$ where N is the number of sources. The data connected with the solid line are those after the corrections for the detection rate and the flux bias. The horizontal error bar gives the flux uncertainty obtained from the simulations, and the vertical error bar includes the uncertainty in the detection rate derived from the simulations. The bottom panels are the same as the top panels, but for cumulative counts. The regions enclosed by the dot lines are constraints derived from a fluctuation analysis on the present data performed in Paper II.

dashed lines are un-corrected counts. The zones enclosed by the dotted lines in the bottom panels are constraints derived from the fluctuation analysis performed on the present survey data in Paper II. It is very encouraging to know that the results from the different methods, i.e., the fluctuation analysis in Paper II and the source extraction in this work, are consistent with each other. It should be noted that the corrections become significant in the flux range below 200 mJy at C_90 and below 250 mJy at C_160, underscoring the importance of the simulations.

Our corrected source counts are compared with other observations and models in Fig. 8. The differential counts for C_90 sources are plotted on the left of the top panels and C_160 sources on the right, and the cumulative counts are given in the middle and bottom panels. The filled circles are from the present work, the open diamonds from the ISO C_90 ELAIS survey (Efstathiou et al. 2000), the “+” (plus) symbols from the IRAS 100 μm counts reported by Efstathiou et al. (2000), the “×” (cross) symbols are from Linden-Vørnle et al. (2000), and the open squares are from the FIRBACK C_160 survey (Dole et al. 2001). The regions enclosed by the dash-dot lines are constraints on the cumulative counts that were derived from the fluctuation analysis in Paper II.

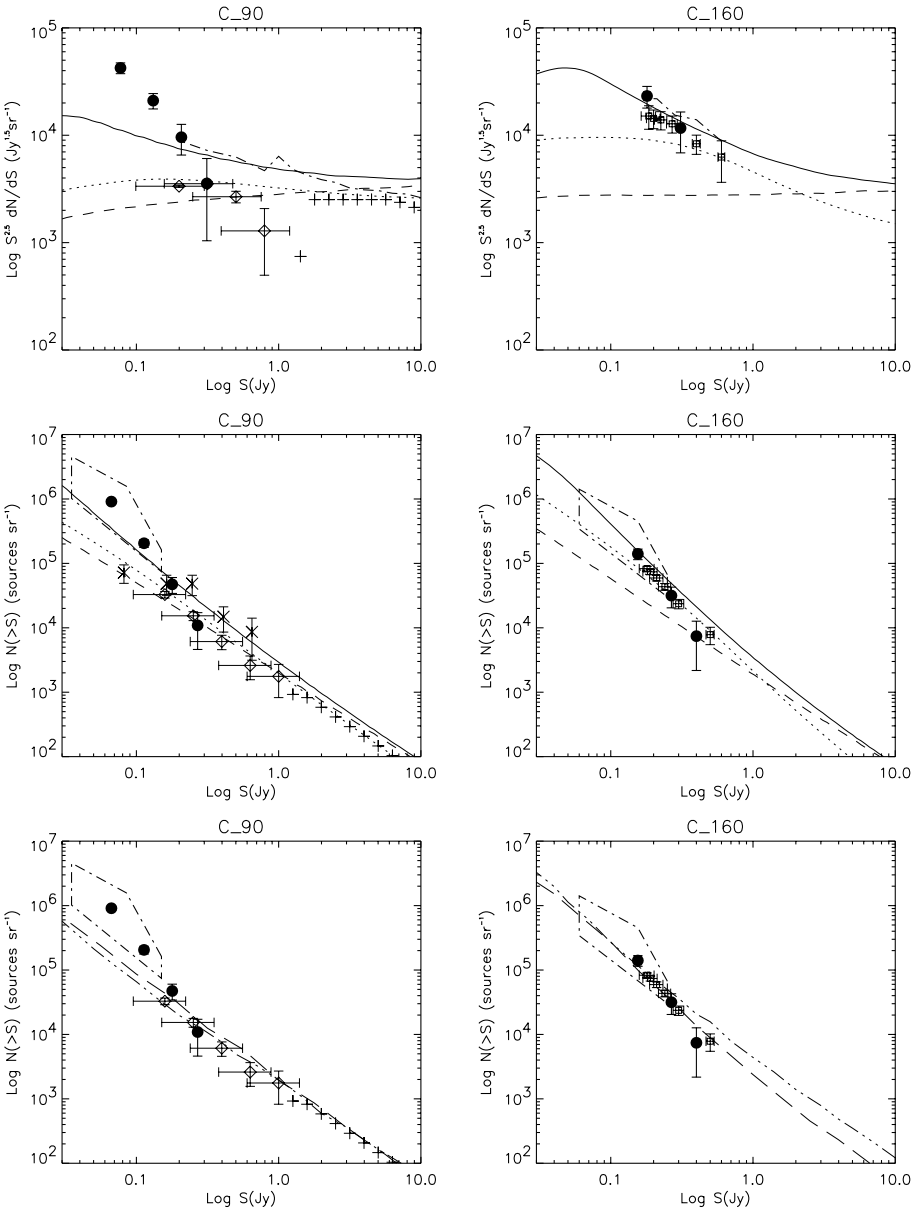

Fig. 8. The number versus flux-density relations for ISO far-infrared sources in the Lockman Hole are compared with other observations and various models. The top panels show the differential counts for C_90 sources on the left and C_160 sources on the right. The filled circles are from the present data after corrections for the detection rate and the flux bias, the open diamonds are from the ISO C_90 ELAIS survey, the plus signs are from the IRAS 100 μm counts by Efstathiou et al. (2000), and the open squares are from the FIRBACK survey (Dole et al. 2001). The solid and dashed lines represent the evolution #3 and no-evolution models by Takeuchi et al. (2001), respectively, the dotted lines represent model E by Guiderdoni et al. (1998), and the dash-dot lines represent a model based on the 15 μm source counts by Chary & Elbaz (2001). The middle panels show the cumulative counts. The filled circles, open diamonds, plus signs, and open diamonds are the same as in the top panels. The “×” symbols are from Linden-Vørnle et al. (2000). The regions enclosed by the dash-dot lines represent constraints from a fluctuation analysis that was performed on the present data in Paper II. The solid, dashed, and dotted lines are the same as in the top panels. The bottom panels are the same as the middle panels, except for the long-dashed and dash-dot-dot lines which represent the models by Rowan-Robinson (2001) and by Franceschini et al. (2001), respectively.

As can be seen in the right panels, our C_160 counts are consistent with the results by Dole et al. (2001). The essence of our work is shown in the left panels. It is clear that our C_90 observations are 2–3 times deeper than those previously published and that there is an upturn in the count slope at ∼200 mJy for C_90 which has never been recognized with the depth of the previous surveys. To explore the nature of the sources, the source counts are compared with various models. The dash-dot lines in the top panels show the model by Chary & Elbaz (2001), based on the differential number counts at 15 μm, especially the “knee” in the count slope at 0.4 mJy (Elbaz et al. 1999). Far-infrared counts are predicted by utilizing the correlations between far-infrared and 15 μm fluxes. In their model, the SFR density peaks at $z = 0.8$ with a value 30× greater than the local value, and gradually decreases towards higher redshift. The solid and dashed lines in the top and middle panels represent the evolution #3 and no-evolution models by Takeuchi et al. (2001), respectively, where they assumed a spike in the star formation history; the SFR density peaks at $z = 0.5$–0.8 where it is 30× greater than in the local universe, while at higher redshift it is only 3× the local value to be consistent with the CIB. The dotted lines illustrate the model of scenario E by Guiderdoni et al. (1998) that yields the maximum counts of far-infrared sources among their models. In scenario E, the SFR density is 3× the local value at $z \sim 0.5$ and peaks at $z \sim 2.5$ with a density of 10× the local value. The models by Rowan-Robinson (2001) and Franceschini et al. (2001) are overlaid in the bottom panels by using the long-dashed and dash-dot-dot lines, respectively. In the models by Rowan-Robinson and Franceschini et al., the SFR densities rapidly increase with redshift, from peaks at $z \sim 1$. The densities are ∼6× the local value at $z = 0.5$, and ∼20× the local value at $z = 1$.

While the models give a reasonable fit to the C_160 counts, all of them, except for the one by Chary & Elbaz (2001), fail to account for the upturn in the C_90 counts. Unfortunately, Chary & Elbaz (2001) only plotted the prediction down to 200 mJy at 90 μm. The model by Takeuchi et al. (2001) is also consistent with the C_90 counts down to 200 mJy, but it underestimates the differential counts by a factor of three at 100 mJy. The model by Takeuchi et al. (2001) is characterized by a spike in the star formation history – the luminosity density from $z = 0.5-0.8$ is 20× the local value. Thus a spike with a three times higher (60× the local value) and a 3× narrower redshift range, for example from $z = 0.5-0.6$, would be worth exploring. If the upturn in the C_90 counts is caused by ultraluminous IR galaxies, their redshifts would be at $z \sim 0.5$. It is urgent to identify the optical counterparts of the faint C_90 sources because these sources would result from a major event of galaxy evolution at moderate redshift. Unfortunately, our C_90 survey is the only ISO survey that detects sources to a depth of 100 mJy at C_90. Thus, it is not clear whether the C_90 upturn can be seen in all directions or if it is specific to the direction of our fields and we are just looking at the high density part of the large scale structure of the galaxy distribution. In future missions such as SIRTF and ASTRO-F, surveys in similar bands are planned and thus should add further information on such questions. Our survey using a 60 cm diameter aperture telescope is heavily limited by the confusion noise due to the high density of far-infrared emitting galaxies, and the correction for the effect of the source confusion is significant, hampering further insight on the nature of sources detected in our survey. For SIRTF and ASTRO-F, with telescope diameters similar to ISO, the super-resolution technique with a carefully designed sampling density would minimize such confusion. Otherwise, we must wait for the Herschel 3.5 m telescope and the SPICA 3.5 m telescope being planned by ISAS.

7. Summary and conclusions

An ISO deep far-infrared survey was conducted in the C_90 (reference wavelength of 90 μm) and C_160 (170 μm) bands in two fields of the Lockman Hole (LHEX and LHNW), covering a combined area of ∼0.9 deg^2. This paper presents the catalogs and source counts. Paper I discussed image processing and reported initial results, while Paper II used a fluctuation analysis of the brightness distribution to derive constraints on the source counts. A summary of the results presented in this paper follows:

- The IRAF DAOPHOT package was used to detect and measure sources.
- Flux calibration was performed using IRAS F10507+5723 (Sb galaxy UGC 06009). The errors associated with this IRAS based calibration are estimated to be 50% at C_90 and 65% at C_160.
- The catalogs were constructed, selecting 223 C_90 sources and 72 C_160 sources with $SNR > 3$, where the error includes the confusion noise due to the high source density.
- Simulations were performed by adding artificial sources in order to estimate the detection rate, the flux bias due to Eddington/Malmquist bias, the positional accuracy, and the total noise including the confusion noise due to the high source density.
- The distribution of the observed associations between C_90 and C_160 sources indicates that the 1σ positional errors are 20″ and 35″ at C_90 and C_160, respectively, which agrees with the results from the simulations.
- The total noise in our observations is dominated by the confusion noise due to the high source density. The confusion noise is ∼20 mJy at C_90 and ∼35 mJy at C_160 which is much larger than the instrumental noise which is at the level of a few mJy or less.
- Corrections for the detection rate and the flux bias are significant for sources fainter than 200 mJy at C_90 and 250 mJy at C_160.
- Most of the sources detected both at C_90 and C_160 have a F(C_160)/F(C_90) color redder than the Sb galaxy UGC 06009. Such a red color could result from reddening by the flux bias or K-correction brightening at C_160 due to the effect of redshift. Red sources brighter than 200 mJy at C_160 may be very luminous galaxies like Arp 220 at moderate redshift.
- The source counts are derived by applying the corrections for the detection rate and flux bias. The resultant counts are quite consistent with those derived from the fluctuation analysis performed in Paper II.
- Our C_160 counts are consistent with the results of Dole et al. (2001).
- Our C_90 observations are 2–3 times deeper than those previously published, and there is an upturn in the count slope at around 200 mJy at C_90 which was not previously recognized given the depth of the previous surveys.
- While recent models give a reasonable fit to the C_160 counts, none of them are successful in accounting for the upturn at the C_90 counts. If the upturn was caused by ultraluminous IR galaxies, their redshifts would be at $z \sim 0.5$, implying a major event of galaxy evolution at moderate redshift.

Acknowledgements. We would like to thank the ISOPHOT team, in particular Carlos Gabriel for many helpful discussion. T. T. Takeuchi has kindly made his models available in differential count form.

References

Acosta-Pulido, J. A., Babriel, C., & Castañeda, H. O. 1999, Transients effects in ISOPHOT data, http://www.iso.vilspa.esa.es/users/expl_lib/PHT_list.html

Altieri, B., Metcalfe, L., Kneib, J. P., et al. 1999, A&A, 343, L65

Alton, P. B., Trewhella, M., Davies, J. I., et al. 1998, A&A, 335, 807

Aussel, H., Cesarsky, C. J., Elbaz, D., & Starck, J. L. 1999, A&A, 342, 313

Barger, A. J., Cowie, L. L., Sanders, D. B., et al. 1998, Nature, 394, 248

Chary, R., & Elbaz, D. 2001, ApJ, 556, 562

Davis, L. E. 1994, A Reference Guide to the IRAF/DAOPHOT Package, http://iraf.noao.edu/iraf/web/docs/recommend.html

Dale, D. A., Helou, G., Contursi, A., Silbermann, N. A., & Kolhatkar, S. 2001, ApJ, 549, 215
Dole, H., Gispert, R., Lagache, G., et al. 2001, A&A, 372, 364
Efstathiou, A., Oliver, S., Rowan-Robinson, M., et al. 2000, MNRAS, 319, 1169
Efstathiou, A., Rowan-Robinson, M., & Siebenmorgen, R. 2000, MNRAS, 313, 734
Elbaz, D., Cesarsky, C. J., Fadda, D., et al. 1999, A&A, 351, L37
Flores, H., Hammer, F., Désert, F. X., et al. 1999, A&A, 343, 389
Flores, H., Hammer, F., Thuan, T. X., et al. 1999, ApJ, 517, 148
Franceschini, A., Aussel, H., Cesarsky, C. J., Elbaz, D., & Fadda, D. 2001, A&A, 378, 1
Gabriel, C., Acosta-Pulido, J., & Kinkel, U. 1997, Proc. of the ADASS VI Conf., ed. G. Hugg, & H. E. Payne, 108
Gautier, T. N. III, Boulanger, F., Pérault, M., & Puget, J.-L. 1992, AJ, 103, 1313
Guiderdoni, B., Bouchet, F. R., Puget, J.-L., Lagache, G., & Hivon, E. 1997, Nature, 390, 257
Guiderdoni, B., Hivon, E., Bouchet, F. R., & Maffei, B. 1998, MNRAS, 295, 877
Haas, M., Lemke, D., Stickel, M., et al. 1998, A&A, 338, L33
Hasinger, G., Burg, R., Giacconi, R., et al. 1998, A&A, 329, 482
Hauser, M. G., & Dwek, E. 2001, ARA&A, 39, 249
Helou, G., & Beichman, C. A. 1990, in Proc. of Liège Symp. on Submillimeter Astronomy, 117
Hogg, D. W. 2001, AJ, 121, 1207
Hughes, D. H., Serjeant, S., Dunlop, J., et al. 1998, Nature, 394, 241
IRAS FSC, version 2.0, 1990, Joint IRAS Science Working Group, U.S. Government Printing Office, Washington D.C.
ISO Handbook Volume V(PHT), SAI/99-069/Dc, Version 1.0, February 2000 http://isowww.estec.esa.nl/manuals/pht_idum41/pidum41/
Juvela, M., Mattila, K., & Lemke, D. 2000, A&A, 360, 813
Kawara, K., Sato, Y., Matsuhara, H., et al. 1998, A&A, 336, L9 (Paper I)
Kessler, M. F., Steinz, J. A., Anderegg, M. E., et al. 1996, A&A, 315, L27
Kiss, Cs., Ábrahám, P., Klass, U., Juvela, M., & Lemke, D. 2001, A&A, 379, 1161
Klaas, U., Hass, M., Heinrichsen, I., & Schulz, B. 1997, A&A, 325, L21
Lagache, G., & Puget, J. L. 2000, A&A, 355, 17
Lagache, G., & Dole, H. 2001, A&A, 372, 702
Lemke, D., Klaas, U., Abolins, J., et al. 1996, A&A, 315, L64
Linden-Vørnle, M. J. D., Nørgaard-Nielsen, H. U., Jørgensen, H. E., et al. 2000, A&A, 359, 51
Lockman, F. J., Jahoda, K., & McCammon, D. 1986, ApJ, 302, 432
Madau, P., Ferguson, H. C., Dickinson, M. E., et al. 1996, MNRAS, 283, 1388
Matsuhara, H., Kawara, K., Sato, Y., et al. 2000, A&A, 361, 407 (Paper II)
Okumura, K. 2000, ESA SP-455, 47
Oliver, S., Rowan-Robinson, M., Alexander, D. M., et al. 2000, MNRAS, 316, 749
Oliver, S., Mann, R. G., & Carballo, R. 2002, MNRAS, 332, 536
Puget, J.-L., Abergel, A., Bernard, J.-P., et al. 1996, A&A, 308, L5
Puget, J.-L., Lagache, G., Clements, D. L., et al. 1999, A&A, 345, 29
Pearson, C., & Rowan-Robinson, M. 1996, MNRAS, 283, 174
Rigopoulou, D., Lawrence, A., & Rowan-Robinson, M. 1996, MNRAS, 278, 1049
Rowan-Robinson, M. 2001, ApJ, 549, 745
De Ruiter, H. R., Zamorani, G., Parma, P., et al. 1997, A&A, 319, 7
Sanders, D. B., & Mirabel, I. F. 1996, ARA&A, 34, 749
Sato, Y., Cowie, L. L., Kawara, K., et al. 2002, ApJ, 578, L23
Sato, Y., Kawara, K., Cowie, L. L., et al. 2003, A&A, 405, 833
Serjeant, S. B. G., Eaton, N., Oliver, S. J., et al. 1997, MNRAS, 289, 457
Scott, S. E., Fox, M. J., Dunlop, J. S., et al. 2002, MNRAS, 331, 817
Smail, I., Ivison, R. J., & Blain, A. W. 1997, ApJ, 490, L5
Soifer, B. T., & Neugebauer, G. 1991, AJ, 101, 354
Steidel, C. C., Adelberger, K. L., Giavalisco, M., Dickson, M., & Pettini, M. 1999, ApJ, 519, 1
Stetson, P. B. 1987, PASP, 99, 191
Takeuchi, T. T., Ishii, T. T., Hirashita, H., et al. 2001, PASJ, 53, 37
Taniguchi, Y., Cowie, L. L., Sato, Y., et al. 1997, A&A, 328, L9
Thuan, T. X., & Sauvage, M. 1992, A&AS, 92, 749